Comparison of the Lifting Line Free Vortex Wake method and the Blade Element Momentum method for the unsteady aerodynamics of a 15MW FOWT

F.M.A de Ridder

Master Thesis

Comparison of the Lifting Line Free Vortex Wake method and the Blade Element Momentum method for the unsteady aerodynamics of a 15MW FOWT

Master of Science Thesis

by

F.M.A. de Ridder

to obtain the degree of Master of Science in Sustainable Energy Technology at Delft University of Technology

Student number:	4550536
Thesis committee:	Axelle Viré
	Daniel van den Berg
	Pim van der Male

Wind Energy Group, Faculty of Aerospace Engineering, Delft University of Technology

Faculty of Electrical Engineering, Mathematics and Computer Science, Delft University of Technology

An electronic version of this thesis is available at `http://repository.tudelft.nl/`.

Acknowledgements

This thesis concludes my academic journey at TU Delft, where I first earned a bachelor's degree in Mechanical Engineering, followed by a master's in Sustainable Energy Technology. Not only have I gained knowledge, but I have also developed a variety of skills, in and out of academia, that will be valuable in my future career.

I want to start by expressing my gratitude to Axelle Viré for her expertise and guidance throughout this project. Additionally, this endeavor would not have been possible without Daniel van den Berg whose insights and support helped shape my thesis. The weekly meetings were a consistent source of motivation, and I enjoyed our conversations that extended beyond just my work. Lastly, I want to thank Pim van der Male for being on my thesis committee.

Special thanks go to my thesis study buddies —Erik, Fred, Gijs, and Lisa— for making the days at the university far more enjoyable and engaging this past year. Next, I would like to express my heartfelt thanks to my family —Cees, Gerda, Martine, and Annie— for their unwavering support throughout my studies, all the way from Zeeland. Last but not least, I want to thank Don, who entered my life just before I began my thesis and supported me through both the highs and lows.

Femke de Ridder
Delft, October 2024

Abstract

Accurate wind turbine modelling is essential for reliable aerodynamic performance predictions. The industry primarily uses the Blade Element Momentum (BEM) method with correction models, but BEM's assumptions become less valid with larger rotors and in Floating Offshore Wind Turbines (FOWTs), where wave interactions and wake dynamics are more complex. The Lifting Line Free Vortex Wake (LLFVW) method offers higher modelling fidelity but is less computationally efficient.

This study compares a BEM and LLFVW model implemented in the software QBlade. The evaluated parameters include power, torque, thrust, root bending moment, tip deflection, and angle of attack using the floating 15 MW UMaine VolturnUS-S reference turbine under various wind and wave conditions taken from several Design Load Cases (DLCs). The aim is to identify any differences between the methods and the met-ocean conditions under which these are most pronounced.

The results show minimal differences in BEM and LLFVW outputs under varying wave conditions. However, wind conditions have a greater impact, particularly around rated speeds where discrepancies were observed, mainly due to different controller dynamics. Above-rated conditions showed similar power, torque, and thrust predictions, but notable differences in angle of attack. The maximum and standard deviation of the root bending moment and tip deflection were found to be consistently lower for LLFVW compared to BEM.

Contents

List of Figures

List of Tables

Nomenclature

Abbreviations & Acronyms

Abbreviation	Definition
AoA	Angle of Attack
AWSM	Aerodynamic Windturbine Simulation Module
BEM	Blade Element Momentum
BET	Blade Element Theory
BL	Boundary Layer
CFD	Computational Fluid Dynamics
DLC	Design Load Case
DoF	Degree of Freedom
ECN	Energieonderzoek Centrum Nederland
ETM	Extreme Turbulence Model
FOWT	Floating Offshore Wind Turbine
FVW	Free Vortex Wake
HH	Hub Height
JONSWAP	Joint North Sea Wave Observation Project
LE	Leading Edge
LLFVW	Lifting Line Free Vortex Wake
LLT	Lifting Line Theory
MT	Momentum Theory
NREL	National Renewable Energy Laboratory
NTM	Normal Turbulence Model
IEC	International Electrotechnical Commission
OF	OpenFAST
OOP	Out-of-Plane
PM	Pierson-Moskowitz
TE	Trailing Edge
TSR	Tip Speed Ratio
RNA	Rotor-Nacelle Assembly
VRS	Vortex Ring State

Symbols

Symbol	Definition	Unit
A_R	Area of rotor	[m^2]
a	Axial induction factor	[-]
a'	Tangential induction factor	[-]
c	Chord length	[m]
C_D	Drag coefficient	[-]
C_L	Lift coefficient	[-]
C_P	Power coefficient	[-]
C_T	Thrust coefficient	[-]
D	Drag	[N]
F_D	Drag force	[N]
F_L	Lift force	[N]
F_N	Normal force	[N]
F_T	Thrust force	[N]
f_p	Peak frequency	[Hz]
H_s	Significant wave height	[m]
I	Turbulence intensity	[-]
L	Lift	[N]
$\dot{m}$	Mass flow rate	[]
P	Power	[W]
R	Blade radius	[m]
r	Distance in wake	[m]
T	Thrust	[N]
T_p	Peak spectral period	[s]
U	Wind speed	[m/s]
U_∞	Free-stream wind speed	[m/s]
V_{ind}	Induced velocity	[m/s]
V_{rel}	Relative velocity	[m/s]
$\mathbf{x}_t$	Wake node position vector	
α	Angle of Attack	[°]
β	Twist angle	[°]
γ	Yaw angle	[°]
γ	Peak shape parameter	[-]
Γ	Vortex-line strength/circulation	[m^2/s]
θ	Local pitch angle	[°]
θ_p	Global pitch angle	[°]
ϕ	Inflow angle	[°]
λ	Tip speed ratio	[-]
ρ	Air density	[kg/m^3]
ν	Kinematic viscosity	[m^2/s]
σ	Spectral width parameter	[-]
σ	Standard deviation	[-]
Ω	Rotor rotational speed	[m/s]

1

Introduction

In this first chapter, the motivation for the research is given in Section 1.1 followed by the research question and hypothesis in Section 1.2. Lastly, in Section 1.3 the structure of the report is outlined.

1.1. Motivation

Offshore wind is a major contributor to renewable energy production and is instrumental in reducing carbon emissions. Floating Offshore Wind Turbines (FOWTs) hold a promising role by unlocking the potential of deep-water resources that are otherwise inaccessible with bottom-fixed structures. However, to fully realize their potential, accurate modelling of wind turbine performance is crucial for optimization. FOWTs, when compared to bottom-fixed turbines, impose even greater modelling challenges as their dynamics are influenced by the interconnected effects of aerodynamics, hydrodynamics as well as platform and mooring dynamics [1].

Currently, computational codes used in research and industry still largely rely on the simplified, yet fast, Blade Element Momentum (BEM) method and its correction models. Additionally, these models are primarily validated and verified with data from smaller, bottom-fixed wind turbines [2]. However, the simplifications and assumptions inherent in these codes may not suffice as rotor sizes increase and additional motions are introduced as is the case with FOWTs. This highlights the importance of verifying these codes against higher fidelity models to ensure their accuracy and reliability under these more complex conditions. The Lifting Line Free Vortex Wake (LLFVW) method is an example of a higher-fidelity model that explicitly simulates the wake structure around wind turbines, providing more detailed and accurate results. However, the trade-off for this precision is longer simulation times due to the increased computational complexity.

From an economic perspective, accurate modelling of the loads and power production of a FOWT could help indicate the actual cost of wind power [3]. Accurate load modelling is essential for optimizing the structural design and material use in FOWTs. Overestimating loads can lead to over-engineering, resulting in unnecessary costs for materials and construction. Conversely, underestimating loads can compromise structural integrity, leading to higher maintenance costs and reduced operational lifespan. Improved modelling contributes to more efficient maintenance and operation strategies.

Regarding system integration, accurate modelling of FOWT systems is essential for their integration into broader energy systems, including the electrical grid. Different codes might better capture certain dynamic behaviors of FOWTs or the effects of control systems. Understanding these differences through comparative studies helps in developing integrated models that more accurately predict how FOWTs will interact with other grid components, thus enhancing system stability and efficiency.

1.2. Research Question & Hypothesis

The main research question of this thesis is:

Is there a difference between BEM and LLFVW in modelling the aerodynamic performance of a FOWT during unsteady operation, and if so, under which met-ocean conditions are these differences most pronounced?

This question centers around understanding the circumstances under which employing BEM or LLFVW would offer advantages in the context of wind and wave conditions encountered by FOWT's.

The evaluated output parameters include power, torque, thrust, root bending moment, tip deflection, and angle of attack. Analyzing power, torque, and thrust under varying wind and wave conditions reveals how well each method captures turbine performance, especially during non-steady wind and waves conditions. Root bending moments and tip deflections are required for precise load modelling, particularly necessary in the case of FOWTs, where wave-induced motions interact with aerodynamic forces causing more dynamic loading on the structure. The angle of attack, a critical blade characteristic, plays a key role in predicting the onset of stall. This is also important for FOWTs where the turbine can interact with its own wake.

In order to investigate this, two sub-questions are formulated:

What is the dependency on wind conditions?

This question explores how the differences between BEM and LLFVW vary with different wind conditions. It seeks to identify certain wind speed ranges and turbulence characteristics where differences between the methods are most significant.

What is the dependency on wave conditions?

This question is focused on understanding the influence of wave characteristics on the performance of LLFVW versus BEM. It aims to uncover whether certain wave heights, periods, or spectral distributions favor the use of one method over the other, and how these dependencies might affect the overall aerodynamic analysis of FOWTs.

Hypothesis

BEM is known to deliver satisfactory results for the output parameters under mild wind and wave conditions, where wind speeds are steady, turbulence is moderate, and blade deformations are small. In such scenarios, BEM offers a good trade-off between accuracy and computational efficiency, making it ideal for early-stage design work. However, in more extreme conditions, such as unsteady winds, large blade deformations, or high tip speed ratios, BEM's limitations become evident, and higher-fidelity models like LLFVW tend to yield more accurate results. In the case of FOWTs, the turbine can interact with its own wake, complicating the aerodynamic modelling. Since BEM lacks a detailed wake structure model, its accuracy may reduce in these situations, potentially under -or overestimating key aerodynamic effects.

The differences between the predictions of BEM and LLFVW will be more pronounced under varied wind conditions compared to wave conditions. This is attributed to the fact that wind conditions can change rapidly over time, leading to larger variations in aerodynamic performance. In contrast, wave conditions change more slowly, resulting in comparatively smaller variations in turbine behavior over time.

1.3. Outline

The report of this thesis is structured as follows. First, Chapter 2 provides the reader with the required background information on the compared methods as well as the general aerodynamics of FOWTs and the modelling thereof. Next, Chapter 3 details the research methodology by giving a description of the reference turbine, software QBlade, selection of design load cases and numerical set-up. This is followed by the results in Chapter 4 where the simulation results are presented and discussed. Here the sections corresponds to the evaluated output parameter which are power, torque, thrust, root bending moment, tip deflection and angle of attack. The conclusion can be found in Chapter 5, followed by the recommendations for future work in Chapter 6.

2

Background

This chapter provides the necessary background information to contextualize this thesis. In Section 2.1, a general overview of the aerodynamics of FOWTs is provided. Next, Section 2.2 explains the blade element momentum method, followed by Section 2.3, which discusses vortex methods. Previous comparative research between these codes is presented in Section 2.4. Finally, Section 2.5 details the modelling of wind and wave conditions.

2.1. Floating Offshore Wind Turbines

Ongoing research is dedicated to FOWTs, with a significant emphasis on studying rotor aerodynamics. Rotors that are not fixed present more complex aerodynamic challenges due to the movements of the floater. In some cases, rotor blades may interact with their own turbulent wake, resulting in significant and sudden fluctuations in aerodynamic forces. These variations have a more pronounced impact on power output, highlighting the importance of understanding these dynamics in a FOWT context [4].

The combined floating platform motions of a FOWT, especially when considering six degrees of freedom (DoF's), lead to complicated angle of attack fluctuations. The six degrees of freedom entail a combination of translations (surge, sway and heave) and rotations (roll, pitch and yaw) as depicted in Figure 2.1 [3] [5].

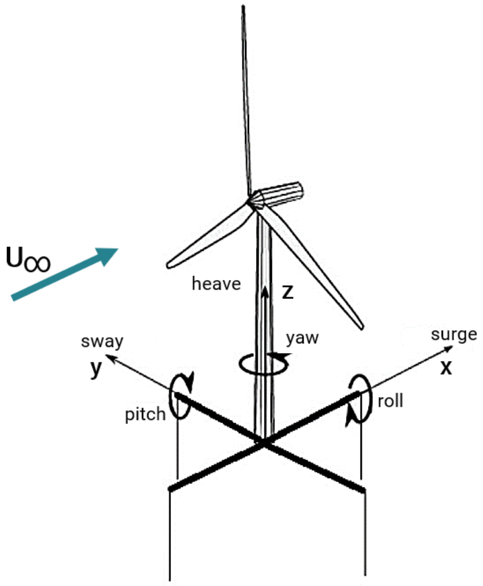

Figure 2.1: Degrees of freedom of a FOWT [6].

Consequently, the FOWT exhibits four distinct operational states, visually represented in Figure 2.2. In the windmill state, the rotor extracts energy from the flow to rotate, causing the streamlines to extend and orderly expand within the wake. Transitioning into a turbulent state, the rotor continues to extract energy from the flow, yet the streamlines become chaotic within the wake. The occurrence of the vortex-ring state (VRS) emerges as the FOWTs rotor moves downwind, resulting in vortex accumulation within the wake, forming a loop around the rotor. Lastly, the propeller state takes place when flow reversal occurs across the rotor, causing the wind turbine to impart energy into the flow similar to a propeller [7][8][9][10].

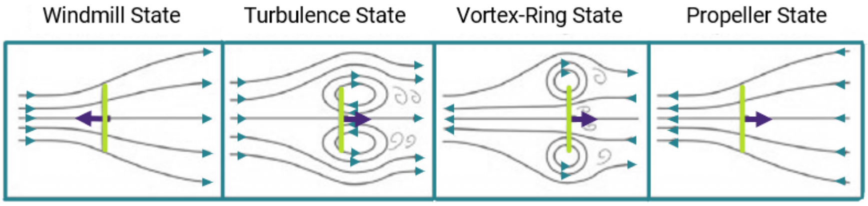

Figure 2.2: The different working states of a FOWT [7].

The additional movements of FOWTs influence the aerodynamics regarding [5]:

- additional mean rotor tilt angle
- varying geometric angle of attack across blade sections
- potential occurrence of vortex ring state
- varying rotor induction (dynamic inflow)
- other effects, such as increased occurrence of skewed inflow and blade-vortex interactions

Numerous studies have already explored how the aerodynamics of a FOWT are affected by platform motions. The amplitudes of both thrust and power coefficients have been found to be influenced by primarily surge and pitch amplitudes [11] [12] [13]. Next to that, unsteady aerofoil effects such as dynamic stall have been observed on FOWTs [14] [15].

Dynamic stall represents a complex fluid dynamics phenomenon witnessed on an airfoil during swift and transient movement when the angle of attack surpasses the static stall angle [16]. It emerges as a viscous event initiated by vorticity buildup near an airfoil's leading edge as the angle of attack rises, bringing the separation point closer to the leading edge. This leads to an initial lift overshoot, succeeded by a sudden decrease in lift as the vortex moves downstream of the airfoil. This sequence forms a hysteresis loop on the $C_L(\alpha)$ curve (Fig.2.3), exhibiting high C_L during the upstroke and low C_L during the downstroke. These dynamics coincide with substantial moment variations due to center of pressure shifts [17].

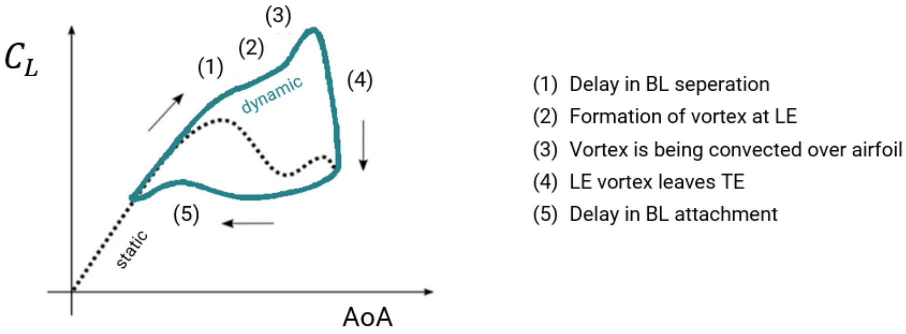

Figure 2.3: The dynamic stall hysteresis loop [18].

In order to model the complex aerodynamics of a FOWT several simulation tools can be of use. These range from the simpler Blade Element Momentum (BEM) method to the more resource-demanding Computational Fluid Dynamics (CFD) models. Vorticity-based methods occupy a middle ground in terms of complexity, computational expenses and the physics-based representation. They offer increased reliability compared to BEM models while demanding lower computational resources than comprehensive CFD models [19]. The BEM method and vortex methods will be explained further in Sections 2.2 and 2.3 respectively.

2.2. Blade Element Momentum Method

The modern form of the BEM theory, as initially formulated by Glauert [20], combines the principles of momentum theory (MT) modelling the induction aerodynamics and blade element theory (BET) modelling the blade aerodynamics. The first linkage is through the relation of the induction factors of the MT with the velocity triangle from BET. The second linkage is equating the elementary thrust and torque obtained from MT and BET [21].

The most important assumptions of the BEM theory are [16][17]:

- Annular independency, axi-symmetry
- stationary, steady flow (non-turbulent)
- inviscid flow
- incompressible flow
- non-yawed conditions
- infinite number of blades

Momentum Theory

The momentum theory models the rotor plane as an actuator disc under the aforementioned assumptions. The basis for this theory is conservation of mass, energy and axial and angular momentum balances [22]. The actuator disc causes a uniform pressure drop over the rotor area while the flow velocity varies continuously through the disc as shown in Figure 2.4. Several actuator disc theories exist, such as the Froude disc (without torque and angular momentum in the wake) and Joukowski disc (with torque and angular momentum in the wake) [23] [24].

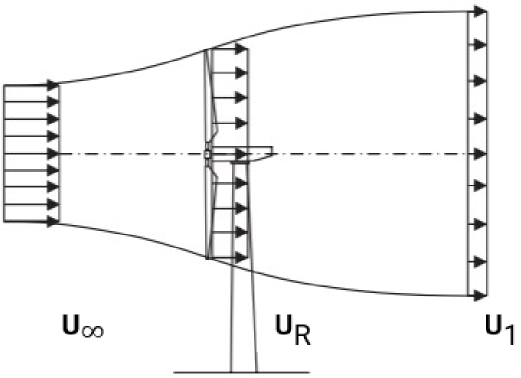

Figure 2.4: The actuator disc theory [25].

The mass flow rate $\dot{m}$ across the stream tube is constant and given below by Eq. 2.1 where ρ is the air density and A the area of the disc at given location.

$$\dot{m} = \rho A_\infty U_\infty = \rho A_R U_R = \rho A_1 U_1 \tag{2.1}$$

The axial induction factor a is introduced as relation 2.2 to describe the velocity deficit caused by the flow deceleration in the rotor plane and can be rewritten as 2.3 or 2.4 [5][25].

$$a = \frac{U_\infty - U_R}{U_\infty} \tag{2.2}$$

$$U_R = (1-a)U_\infty \tag{2.3}$$

$$U_1 = (1-2a)U_\infty \tag{2.4}$$

The power P that can be extracted from the wind is the work rate of the thrust and is written as Eq. 2.5.

$$P = T \cdot U_R = 2\rho U_\infty^3 A \cdot a(1-a)^2 \tag{2.5}$$

The thrust coefficient C_T and the power coefficient C_P can be expressed as a function of the axial induction factor, found in equation 2.6 and 2.7 respectively. The power coefficient is limited by the theoretical Betz limit $C_{P_{max}}$=$\frac{16}{27}$ $\approx$ 0.593 found at a=$\frac{1}{3}$.

$$C_T = \frac{T}{\frac{1}{2}\rho U_\infty^2 A_R} = 4a(1-a) \tag{2.6}$$

$$C_P = \frac{P}{\frac{1}{2}\rho U_\infty^3 A_R} = 4a(1-a)^2 \tag{2.7}$$

Blade Element Theory

The blade element theory divides the blade in a discrete number of radially distributed segments. Based on the assumption that the flow there is locally two-dimensional and in the plane of the airfoil segment, the forces on the blade element can be calculated [26]. The forces and angles of the blade section are depicted in Figure 2.5.

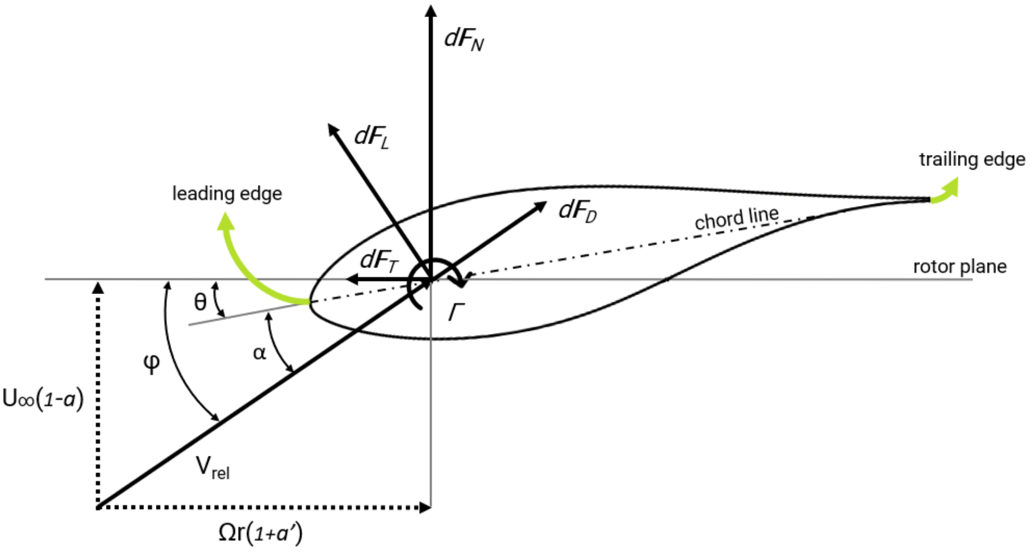

Figure 2.5: Forces acting on blade element.

Eq. 2.8 represents the differential lift force dF_L in terms of the variables air density ρ, relative velocity V_{rel}, lift coefficient C_L, chord length c and differential span element dl. Similarly, the relation for differential drag force dF_D is shown in Eq. 2.9. The lift and drag coefficient are obtainable through tabulated aerodynamic parameters specific to the airfoil at a given angle of attack.

$$dF_L = \frac{1}{2}\rho V_{\text{rel}}^2 C_L(\alpha) c\, dl \tag{2.8}$$

$$dF_D = \frac{1}{2}\rho V_{\text{rel}}^2 C_D(\alpha) c\, dl \tag{2.9}$$

In Eq. 2.10 the angle of attack α is defined as the difference between the inflow angle ϕ and the global pitch angle θ. The global pitch angle (Eq. 2.11) is a combination of the local pitch angle of the blade section θ_p and the twist angle β.

$$\alpha = \phi - \theta \tag{2.10}$$

$$\theta = \theta_p + \beta \tag{2.11}$$

Using the velocity triangle from Figure 2.5 the inflow angle ϕ can be computed with the tangential and axial wind speeds via Eq. 2.12.

$$tan(\phi) = \frac{(1-a)U_\infty}{(1+a')\Omega r} \tag{2.12}$$

The decomposition of lift and drag into components along the longitudinal and rotor planes results in:

$$dF_N = dF_L cos(\phi) + dF_D sin(\phi) \tag{2.13}$$

$$dF_T = dF_L sin(\phi) - dF_D cos(\phi) \tag{2.14}$$

Limitations & Corrections

The constraints inherent in the assumptions upon which BEM is founded limit its applicability in specific scenarios. The model is based on steady flow conditions, hereby disregarding turbulence effects [19]. Furthermore, a limitation of the model is its reliance on empirical input of 2D airfoil data, which may not always be readily accessible [22]. Typically, this data is acquired in wind tunnels at lower Reynolds numbers than those prevalent in today's larger turbines [16]. Explained below are numerous engineering extensions that exist to address the simplifications and underlying assumptions of BEM.

Tip and root loss correction. This correction is needed to account for the finite number of blades. At the blade tip the axial velocity is usually not zero, the flow is largely attached and rotational effects are negligible [27]. This is generally covered with the Prandtl tip loss correction (or modifications, e.g. by Shen [28]) that gives the ratio between local blade induction and the azimuthally averaged induction axial induction [17].

Oblique (or skewed) inflow correction. This correction is necessary to account for the angle between the rotor plane and the incoming wind. A skew function is determined for each element as a function of the effective yaw angle, azimuth angle and radial location. This function relates the local induction at each element to the annulus averaged axial induction [29].

Dynamic inflow correction. This correction aims to account for the fluctuating aerodynamic behavior caused by the delayed wake reaction. The term dynamic inflow is used to indicate the dynamic response of the inflow velocities in the rotor plane, to changes in the load conditions on the rotor [30]. This correction involves integrating low-pass filters onto the quasi-steady induced velocities to capture the unsteady aerodynamic response [31].

Turbulent wake state model. For large values of the axial induction factor (a > 0.5) the stream tube concept becomes invalid, as is the case for heavily loaded rotors [17]. In this case BEM predicts flow reversal in the wake, while in reality the wake transforms into a turbulent state by interacting with air from outside the stream tube [29]. Many corrections are derived from Glauert's approach [32], wherein the momentum equation is substituted with a turbulent wake state equation.

Stall delay model. This correction accounts for the so-called Himmelskamp effect, which indicates that a rotating blade produces higher lift forces compared to a stationary blade, as observed by Himmelskamp [33] (see Fig.2.6). At the inner part of the wind turbine blade there is significant radial flow causing a delay in effective angle of attack at which the airfoil stalls [27]. A commonly used correction is the one of Snel [34] where only the lift and not the drag coefficient needs to be modified.

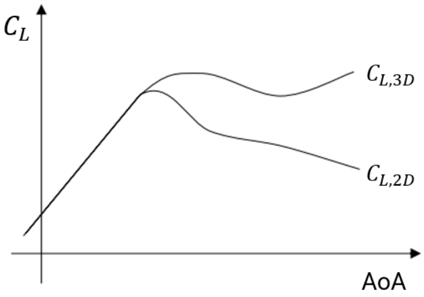

Figure 2.6: Stall delay for a rotating wing ($C_{L,3D}$) compared to a static non-rotating wing ($C_{L,2D}$) [19].

Dynamic stall models. This correction accounts for the phenomenon of dynamic stall in wind turbines where the angle of attack exceeds the static stall angle. Most dynamic stall models are based on the semi-empirical Beddoes-Leishman [35] model or the Øye model [36].

2.3. Vortex Methods

Several so-called vortex methods can be distinguished to model the aerodynamics of FOWTs. Vortex methods represent a specific category within Lagrangian methods, where the tracked quantities are integral values over material volumes and the centroid of each volume moves as a Lagrangian marker.

To reduce dimensions the vorticity can be represented as a sheet, line or particle. The vortex lattice method involves horseshoe vortices positioned along the mid-surface of the rotor blades. Meanwhile, the panel method employs a mesh of vortex rings to model the upper and lower surfaces of the blades. In contrast, the lifting line method represents blades using a single line of vortices situated at the quarter-chord points [37] [21].

Regarding wake modelling, two classes of vorticity-based methods are used. Prescribed wake methods involve the convection of wake elements along a predefined path. On the other hand, free wake methods dynamically update the wake end nodes' positions based on the local velocity, incorporating inflow velocity and induced velocity from all wake elements within the domain. Free wake methods offer higher accuracy by adhering to underlying physical principles to shape the wake, albeit at a significantly higher computational cost compared to prescribed wake methods [37]. In the next section the Lifting Line Free Vortex Wake (LLFVW) theory is discussed.

Lifting Line Free Vortex Wake method

The LLFVW method is based on the following assumptions [21]:

- steady flow
- inviscid flow
- incompressible flow
- irrotational flow

The blades are portrayed using lifting lines at a quarter chord length characterized by equivalent vortex strengths, representing the circulation known as bound vorticity. Within the wake, vorticity is categorized as either shed vorticity, emitted due to the time change in bound circulation, or trailed vorticity, resulting from the spanwise change in bound circulation [26] [38] (see Fig.2.7).

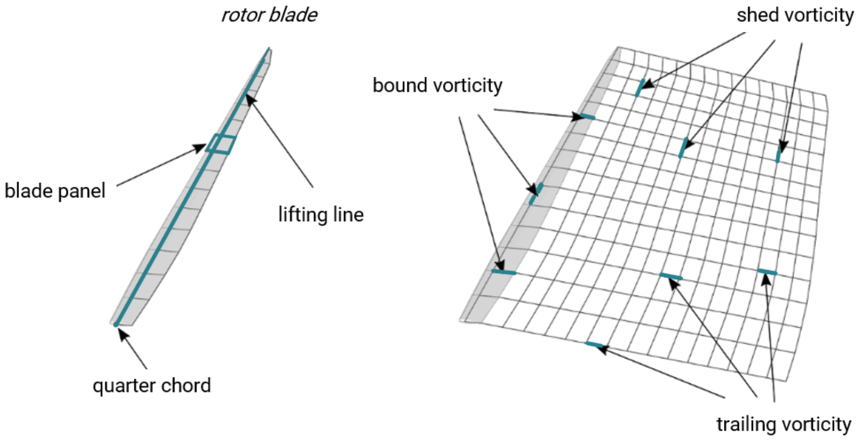

Figure 2.7: The lifting line representation of the blade with bound, shed and trailing vorticity [18].

The Kutta-Joukowski theorem (Eq. 2.15) is used to formulate the sectional circulation:

$$\partial F_L(\alpha) = \rho V_{\text{rel}} \times \partial\Gamma \tag{2.15}$$

This theorem defines the sectional lift force $F_L(\alpha)$ on a vortex segment $d\mathbf{l}$ by the production of the fluid density ρ, the bound vortex strength Γ on the segment, and the relative wind velocity V_{rel} which can be obtained from the velocity triangle [8].

The Biot-Savart law (Eq. 2.16) introduces a causal link between vorticity and velocity. It considers the locations of Lagrangian markers and the intensity of vortex elements. It is used to compute the induced velocity V_{ind} of a vortex filament $d\mathbf{l}$ with constant strength Γ at different points at distance r inside the wake [5][18].

$$V_{\text{ind}} = -\frac{1}{4\pi}\int \Gamma \frac{\mathbf{r} \times d\mathbf{l}}{r^3} \tag{2.16}$$

Comparison with BEM

The primary distinction from BEM lies in the explicit resolution of the rotor wake. The rotor wake is physically modeled in space and time and phenomena like tip roll-up, the dynamic inflow effect and rotor motions into and out of the wake as potentially present for FOWTs are represented without additional engineering correction models [5] [26]. This results in more precise simulations, especially in scenarios where BEM's assumptions are compromised, such as during unsteady operation, significant blade deformations, and high tip speed ratios nearing a turbulent wake state [18]. However, similar to BEM this method relies on the prescription of aerodynamic profile data as function of the angle of attack [17].

2.4. Previous Code Comparison Efforts

In the past researchers have undertaken comparative studies to assess the performance of BEM in comparison to vortex methods, CFD and/or experimental data. Table 2.1 summarizes the most relevant previous code comparison efforts, predominantly featuring the multi-physics software QBlade, a tool integral to this thesis. The main overall conclusions are that:

- BEM performs well in simple situations involving steady wind.
- BEM generally overpredicts loads.
- BEM has trouble with modelling dynamic inflow effects, but performance improves with the dynamic inflow correction.

Publication/Project	**Compared Methods**	**Turbine Rating**	**Main Conclusions**
Hauptmann *et al.* (2014) [29]	BEM & LLFVW	5MW (UpWind)	• LLFVW outperforms BEM in non-axial inflow, yawed, and asymmetrical pitch situations for specific DLCs.
AVATAR project (2018) [39]	BEM & LLFVW	10 MW	• Load cases influenced by induction effects (e.g., yawed cases) pose greater modelling challenges for BEM-based methods compared to external flow driven cases (e.g. sheared cases). LLFVW models both these cases accurately. • Fatigue loads for normal production cases at turbulent inflow were overpredicted by 15% by BEM compared to LLFVW methods.
Perez-Becker *et al.* (2020) [27]	BEM (OF) & LLFWV (QBlade)	10 MW (DTU)	• Higher average aerodynamic torque in LLFWV simulations than BEM. • Lower fatigue loads obtained with LLFWV simulations.
Ramos-García *et al.* (2021) [40]	BEM (HAWC2) & LLFWV (MIRAS-HAWC2)	15 MW (IEA RWT on WindCrete spar-buoy floater)	• Differences between BEM and LL methods are more sensitive to variations in wave frequency than in wave amplitude. • Largest differences between codes during backward motion of rotor and for high wind speeds under regular waves.
Boorsma *et al.* (2022) [41]	BEM & LLFVW & CFD & experimental data	2.3 MW (DTU)	• Axial flow conditions: Good agreement observed among different code types. • Sheared inflow conditions: Uncertainties in rotational effects on airfoil data led to discrepancies, with CFD results standing out above methods using sectional airfoil data. • Yawed flow conditions: modelling of skewed wake effects remained problematic for BEM codes, while CFD and LLFVW codes demonstrated better representation of underlying physics.
FLOATECH D2.2. (2022) [42]	BEM (OF) & LLFVW (QBLade) & experimental data	5 MW OC5 & 10 MW SOFTWIND & 10 MW Hexafloat	• For all three simulated models, good agreement is noted between the codes and the experiments (where present) in tests without wind. • In tests with irregular wind and waves, statistical variations in rotor loads in unsteady wind are discernible when using LLFVW as compared to other BEM-style models.

Publication/Project	**Compared Methods**	**Turbine Rating**	**Main Conclusions**
Behrens de Luna *et al.* (2022) [43]	QBEM & QLLT (QBlade) & HBEM & HLLT & CFD (HAWC2)	10 MW (DTU)	• Purely aerodynamic simulations show the most significant deviation from the CFD code in scenarios with high tip-speed-ratios. • Both BEM-codes consistently overpredicted loads along the outer radius in tangential and normal directions.
OC6 Project (2023) [31]	BEM & LLFVW & CFD	10 MW (DTU)	• Good agreement observed between the numerical models and the experiments for the platform frequencies and amplitudes considered. • Only a small hysteresis in airfoil performance undergoing angle of attack variations in attached flow observed by participants using unsteady airfoil aerodynamics.
Papi *et al.* (2023) [44]	BEM & DBEM & LLFVW & ALM & experimental data	10 MW (DTU) & UNAFLOW rotor	• Similarity between BEM and higher order theories in simple surge oscillations. • Attributes the similarity to the way induced velocity and structural velocity variations combine along the blade span.
Behrens de Luna *et al.* (2024) [45]	BEM & LLFVW	5 MW OC5 & 10 MW SOFTWIND & 10 MW Hexafloat	• Largest differences seen were related to the application of distinct aerodynamic and structural models on the Hexafloat FOWT.

Table 2.1: Previous code comparison research.

2.5. Met-Ocean Conditions

The met-ocean conditions refer to the collective impact of meteorology and oceanography. These conditions play pivotal roles in simulating the aerodynamics of FOWTs.

Wind Conditions

Modelling wind conditions can range from uniform to fully turbulent wind fields. In the international standard IEC61400-1 Ed-3, the Normal Turbulence Model (NTM) is introduced to characterize turbulence during normal operational conditions. The turbulence intensity is given by Eq. 2.17 with σ the standard deviation of the velocity fluctuations and $\overline{U}$ the mean wind speed. It quantifies how much the wind speed fluctuates around its average value.

$$I = \frac{\sqrt{u'^2}}{u_{\text{ave}}} = \frac{\sigma}{\overline{U}} \tag{2.17}$$

Assuming a normal distribution of turbulence standard deviation, the 90th percentile of the turbulence standard deviation can be represented as [46]:

$$\sigma_{\text{NTM}} = \sigma_{90} = \overline{\sigma} + 1.28\sigma_{\sigma} \tag{2.18}$$

Here $\overline{\sigma}$ is the estimated turbulence standard deviation and σ_{σ} the standard deviation of estimated turbulence standard deviation. The definitions of these parameters are given in Eq. 2.19 and Eq. 2.20 respectively.

$$\overline{\sigma} = I_{\text{ref}}(a\overline{U} + b) \tag{2.19}$$

$$\sigma_{\sigma} = I_{\text{ref}}(\alpha\overline{U} + \beta) \tag{2.20}$$

Here $\overline{U}$ is the averaged wind speed over 10 minutes at hub height. I_{ref} is the expected value of hub height turbulence intensity at a 10 minutes average wind speed of 15 m/s and varies per turbine class. The parameters a, b, α and β are fixed model parameters based on observations and given in table 2.2 [47]. The turbulence for the NTM is then given by equation 2.21.

$$I_{90} = \frac{\sigma_{90}}{\overline{U}} = I_{\text{ref}}\left[a + 1.28\alpha + \frac{(b + 1.28\beta)}{\overline{U}}\right] \tag{2.21}$$

IEC Class	I_{ref}	a	b	α	β
A	0.16	0.75	3.8	0	1.4
B	0.14				
C	0.12				

Table 2.2: Parameters for NTM [46].

The Extreme Turbulence Model (ETM) is presented to model rare wind conditions with extreme turbulence. The definition of the ETM is given as [48][49]:

$$\sigma_{\text{ETM}} = cI_{\text{ref}}\left[0.072\left(\frac{U_{\text{ave}}}{c} + 3\right)\left(\frac{\overline{U}}{c} - 4\right) + 10\right] \tag{2.22}$$

Here U_{ave} is the annual averaged wind speed at hub height and c is a constant of 2 m/s.

Wave Conditions

Most waves originate from wind, although planetary forces or seismic activity, such as earthquakes, can also generate waves. Three important factors dictate the amount of energy transferred from wind to waves, consequently influencing wave size [50]:

1. Wind speed
2. Duration of wind, representing how long the wind persists continuously over the water
3. Fetch, denoting the distance over which the wind blows across the water in a consistent direction

Similar to wind, wave conditions can be modeled with varying levels of complexity. This spans from linear waves to multi-directional irregular waves. Linear waves, also called Airy waves, can be applied under the assumptions that the sea water is incompressible, inviscid and irrotational along with a very small wave steepness [51]. The approach assigns a velocity potential for finite depth.

Irregular wavefields can be modeled using spectra that describe the statistical distribution of wave energy in ocean waves. Two frequently employed wave spectra include the JONSWAP spectrum and the Pierson-Moskowitz spectrum, also referred to as the ISSC spectrum. The latter describes waves in a fully developed sea, where wind blows consistently over a large area for an extended period. In such conditions, the peak shape parameter γ is typically equal to 1. During the Joint North Sea Wave Observation Project (JONSWAP) it was found that the sea is never fully developed. Therefore, an additional factor was introduced to the Pierson-Moskowitz spectrum to better align with their observations [52].

The Pierson-Moskowitz spectrum is described by the Eq. 2.23, while the JONSWAP spectrum is described by Eq. 2.24. These equations are illustrated in Figure 2.8.

$$S_{PM}(\omega) = \frac{5}{16}(\frac{f}{f_p})^{-5} H_s^2 T_p e^{-\frac{5}{4}(\frac{f}{f_p})^{-4}} \tag{2.23}$$

$$S_{JS}(\omega) = A_\gamma S_{PM}(\omega) \gamma^{e^{-\frac{1}{2}\left(\frac{f-f_p}{\sigma f_p}\right)^2}} \tag{2.24}$$

Where:

- T_p is the peak period
- f_p is the peak frequency
- H_s is the significant wave height
- A_γ is a normalizing factor
- γ is the peak shape parameter
- σ is the spectra width parameter

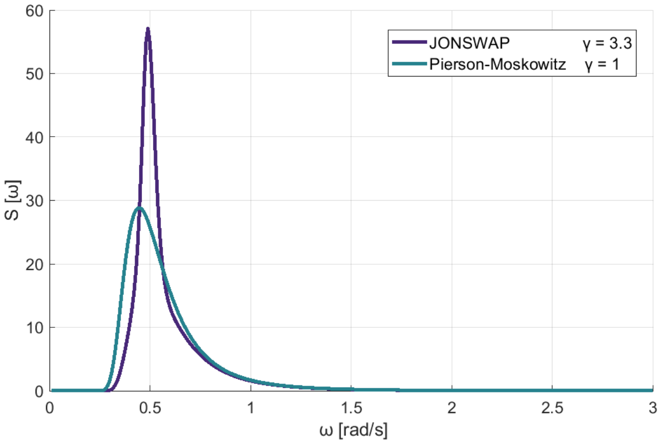

Figure 2.8: JONSWAP and PM spectrum.

Three main factors can be used to describe the wave spectrum. The significant wave height H_s is defined as the average height of the highest third of the wave amplitude, as illustrated in Figure 2.9 [51]. The peak period T_p is the wave period with the highest energy [53]. The peak shape factor γ describes the peak of the spectrum.

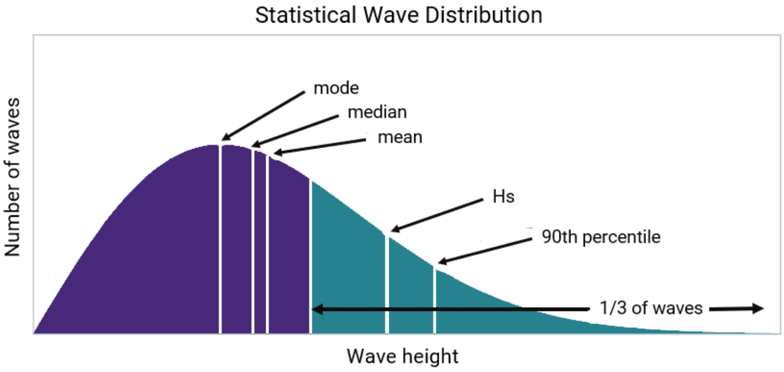

Figure 2.9: Statistical wave distribution [50].

3

Methodology

This chapter gives an overview of the research methodology. It begins with a description of the reference turbine in Section 3.1. Following this, Section 3.2 introduces the physics software QBlade. Next, the design load cases that are selected for simulations are found in Section 3.3. A convergence study on blade panels and wake zone configuration is carried out and the results are shown in Section 3.4. Lastly, the numerical set-up is detailed in Section 3.5.

3.1. VolturnUS-S Reference Turbine

The FOWT used in this study is the floating 15 MW UMaine VolturnUS-S reference turbine [54] shown in Figure 3.1. It is a semi-submersible floating turbine based upon the IEA 15MW offshore reference turbine [55]. The main system properties of the IEA reference turbine are summarized in Table 3.1 and of the VolturnUS-S floater in Table 3.2.

Parameter	Value	Units
Turbine rating	15	[MW]
Turbine class	IEC Class 1B	[-]
Number of blades	3	[-]
Cut-in wind speed	3	[m/s]
Rated wind speed	10.59	[m/s]
Cut-out wind speed	25	[m/s]
Minimum rotor speed	5.0	[rpm]
Maximum rotor speed	7.56	[rpm]
Maximum tip speed	95	[m/s]
Rotor diameter	240	[m]
Airfoil series	FFA-W3	[-]
Hub height	150	[m]
Hub diameter	7.94	[m]
Hub overhang	11.35	[m]
Rotor precone angle	-4.0	[deg]
Blade prebend	4	[m]
Blade mass	65	[t]

Table 3.1: System properties of the 15 MW IEA reference turbine [55].

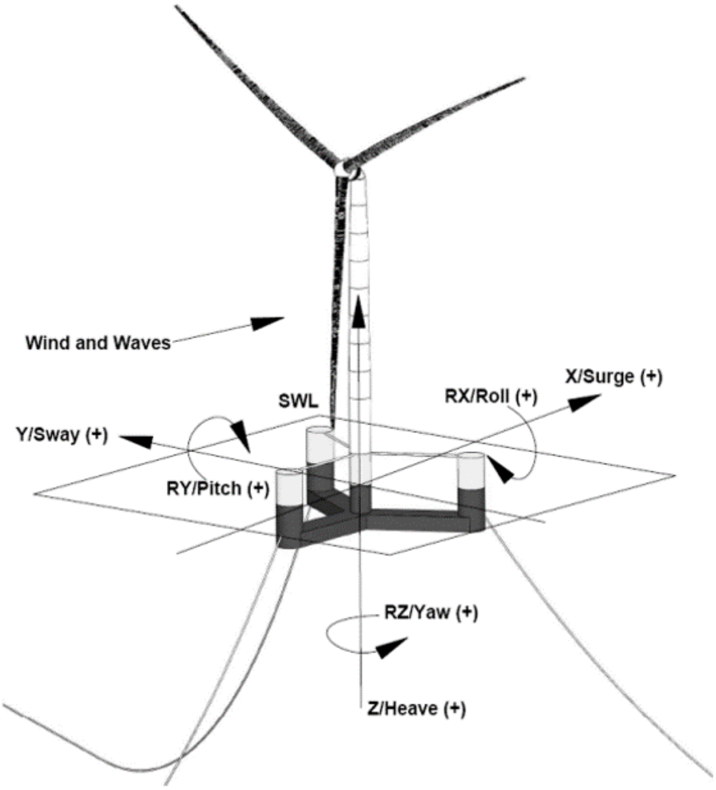

Figure 3.1: The 15 MW VolturnUS-S reference turbine [54].

Parameter	Value	Units
Platform type	semi-submersible	[-]
Total system mass	20,093	[t]
Platform mass	17,839	[t]
Tower mass	1,263	[t]
RNA mass	991	[t]
Water depth	200	[m]
Mooring system	Three-line chain catenary	[-]

Table 3.2: System properties of the VolturnUS-S platform [54].

3.2. QBlade

QBlade is a multi-physics solver that can perform coupled aero-servo-elastic simulations [56]. Both a LLFVW and an unsteady BEM model are available in QBlade and will be used for the comparison in this thesis.

Lifting Line Free Vortex Wake

In QBlade the LLFVW algorithm is implemented to model the aerodynamic forces on the rotor, roughly following the work from van Garrel [57] for the AWSM project. As explained before, the rotor is depicted using a lifting line situated at the quarter chord position of the 2D airfoil sections. Each blade panel is symbolized by a vortex ring comprising four straight vortex filaments. Determination of the circulation in the bound vortex lines, which constitute the lifting line, relies on computed values derived from the relative inflow velocity and the lift and drag coefficients obtained from referenced airfoil data tables.

A simple Euler forward integration scheme is implemented in the QBlade code as a first-order method:

$$\mathbf{x}_{t+1} = \mathbf{x}_t + (V_\infty + V_{\text{ind}}(\mathbf{x}_t))\Delta t \tag{3.1}$$

As a second-order integration method, a predictor corrector that re-evaluates the induced velocity based on the predicted position 3.1.

$$\mathbf{x}_{t+1,\text{cor}} = \mathbf{x}_t + (2V_\infty + V_{\text{ind}}(\mathbf{x}_t) + V_{\text{ind}}(\mathbf{x}_{t+1}))\frac{\Delta t}{2} \tag{3.2}$$

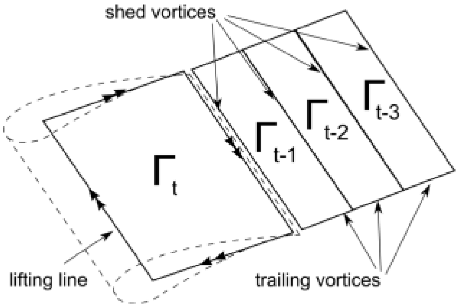

Figure 3.2: Geometry of a blade panel, lifting line positions and shed and trailing vortices [37].

$$\Gamma_{\text{trail}} = \frac{\partial \Gamma_{\text{bound}}}{\partial x}\Delta x \tag{3.3}$$

$$\Gamma_{\text{shed}} = \frac{\partial \Gamma_{\text{bound}}}{\partial t}\Delta t \tag{3.4}$$

The evaluation of the Biot-Savart equation needs to be conducted across:

$$N_{\text{nodes}} * N_{\text{vortices}} \approx \frac{N_{\text{vortices}}^2}{2} \tag{3.5}$$

Vortex Core Desingularization

Vortex core growth models are integrated into the free-wake code to resolve the singularity issue associated with the Biot-Savart law at r = 0 [6]. The vorticity tends to infinity as r approaches zero. The QBLade algorithm uses a cut-off radius r_c as proposed by van Garrel [57].

The adjustment of the core size occurs at each time step in accordance with equation 3.6 where $a = 1.2563$ is a constant, δ_v is the turbulent viscosity coefficient (dependent on rotor size), ν is the kinematic viscosity and Δt is the step size.

$$r_c = r_0 + \sqrt{\frac{4a\delta_v\nu\Delta t}{1+\epsilon}} \tag{3.6}$$

The desingularized Biot-Savart equation then becomes:

$$V_{\text{ind}} = -\frac{1}{4\pi}\int \Gamma \frac{\mathbf{r} \times d\mathbf{l}}{r^3 + r_c^2} \tag{3.7}$$

Polar unsteady BEM

In QBlade turbine simulations can be done using unsteady BEM which is the classical BEM theory enhanced by several correction models.

In QBlade the correction models are:

- Prandtl Tip Loss Factor
- 3D Correction

In the 3D correction, a non-rotating coordinate system is placed at the bottom of the tower and nacelle. Additionally, a coordinate system is fixed to the rotating shaft and each blade. This enables the determination of the instantaneous velocity experienced by each blade, allowing for its incorporation in the calculation of the flow angle [58]. Since classical BEM is applicable to steady flow scenarios and provides induced velocities tailored to such conditions, a dynamic inflow model is employed to introduce a time lag to the sectional rotor induction [59].

Next to these correction models, a polar grid is introduced that divides the annular ring into stationary azimuthal sections [60] (see Fig. 3.3). Each point on the azimuthal grid corresponds to a local induction factor determined by the local instantaneous velocity. This velocity approximation is based on the induced velocity of the neighboring two blades and is weighted by their azimuthal distance [43].

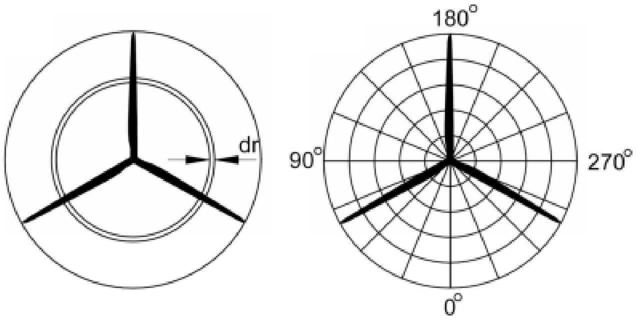

Figure 3.3: The classic approach (left) and the polar grid approach (right) [60].

3.3. Design Load Case Selection

The simulations are based on a set of Design Load Cases (DLCs) outlined in [54], chosen to mirror the diverse operational scenarios encountered by the FOWT during its service life. Table 3.3 provides an overview of a selection of these DLCs. Each DLC encompasses a range of wind speeds coupled with distinct turbine models: NTM for DLC 1.1 and 1.6, and ETM for DLC 1.3. Additionally, DLC 1.6 features elevated wave conditions compared to other DLCs. The wind speeds at hub height are selected to examine conditions below rated conditions (4 m/s) and above it (18 m/s). Mean wind speeds of 8 and 10 m/s are near the rated wind speed, which is 10.59 m/s. Lastly, DLC 6.3 represents the extreme conditions expected over a one-year timeframe, including an additional setting of 20 degrees yaw. The mean wind speed for this DLC is 38 m/s which means the turbine is in parked conditions.

DLC	Wind Condition	HH Mean Wind Speed [m/s]	Significant Wave Height [m]	Peak Spectral Period [s]	Gamma Shape [-]	Additional Setting
1.1	NTM	4.00	1.10	8.52	1.00	
		8.00	1.32	8.01	1.00	
		10.00	1.54	7.65	1.00	
		18.00	3.06	8.05	1.59	
1.3	ETM	4.00	1.10	8.52	1.00	
		8.00	1.32	8.01	1.00	
		10.00	1.54	7.65	1.00	
		18.00	3.06	8.05	1.59	
1.6	NTM	4.00	6.30	11.50	2.75	
		8.00	8.00	12.70	2.75	
		10.00	8.10	12.80	2.75	
		18.00	9.80	14.10	2.75	
6.3	EWM 1 yr	38.00	6.98	11.70	2.75	+/- 20° yaw

Table 3.3: Design load case selection [54].

3.4. Convergence Study

The computational time for FVW simulations is heavily influenced by the number of vortex elements in the wake. This starts with how the blade is divided into panels, as the number of panels determines the amount of vortex filaments released into the wake.

In QBlade, two additional wake settings play a important role. The first is the wake zone configuration, which controls the length of different wake zones in revolutions. As the wake transitions between zones, vortex elements are adjusted by interpolating and replacing them with representative new ones [61], guided by the second setting, the wake zone factor. This factor controls the coarsening level between zones; for example, a factor of two merges every two wake elements into one during transitions, reducing wake resolution but enhancing computational efficiency. Figure 3.4 illustrates the wake zones and the according wake zone factors.

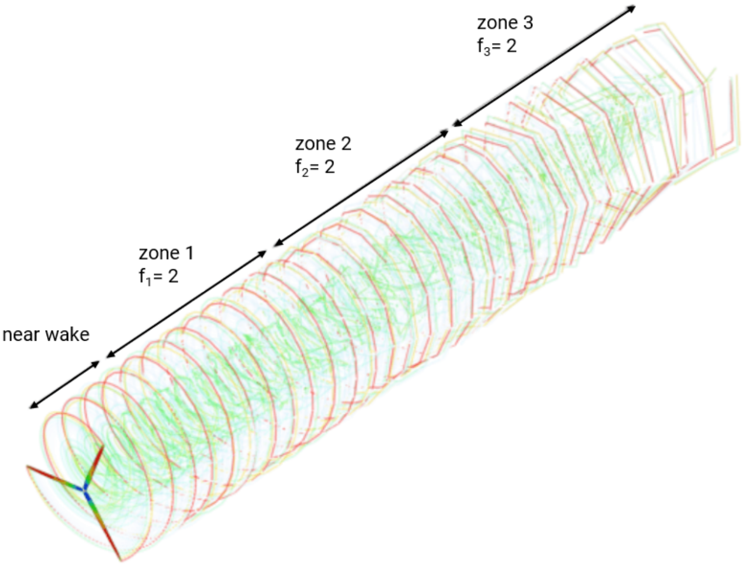

Figure 3.4: Wake zone configuration and wake factors [18].

A convergence study is performed to determine the optimal balance between accuracy and runtime by varying the number of blade panels and the configuration of the wake zones. Two parameters are examined: the turbine thrust (an instantaneous parameter) and the root bending moment (an integrated parameter). The wind and wave field spans a duration of 600 seconds with conditions from DLC 1.1 with a mean hub height wind speed of 8 m/s as can be found in Table 3.3.

For blade panels, the baseline consists of 30 panels which is expected to provide a precise representation. The other discretizations are normalized by this baseline. For wake zone configuration, the baseline for the convergence study is 2/4/6 revolutions per wake transition and the near wake is kept at 0.5 revolution. The other configurations are normalized by this baseline. Furthermore, the wake zone factor is kept at 2 for all wake zones. The results are shown in figure 3.5 and figure 3.6. Opting for 20 blade panels and a 2/2/2 wake zone configuration strikes the optimal balance between computational efficiency and precision.

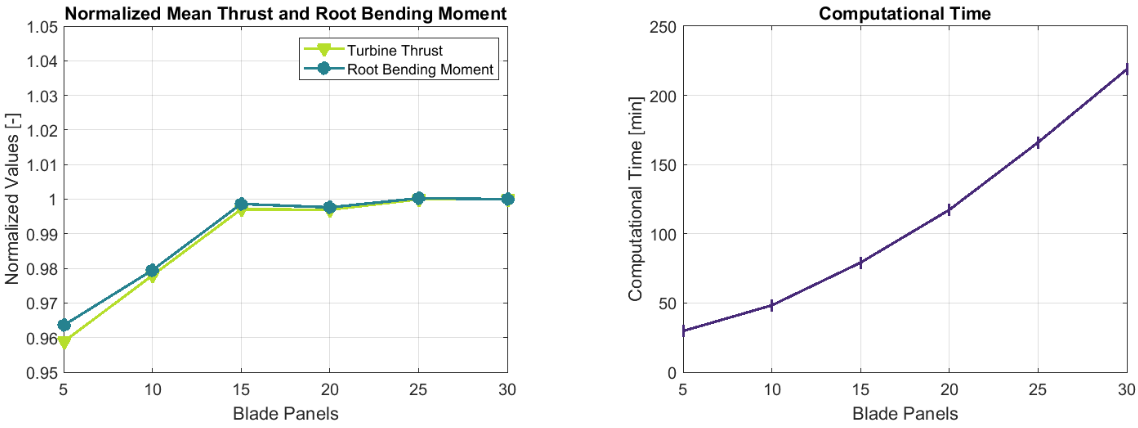

(a) Normalized mean thrust and mean root bending moment.

(b) Computational time.

Figure 3.5: Comparison of different blade panel discretizations.

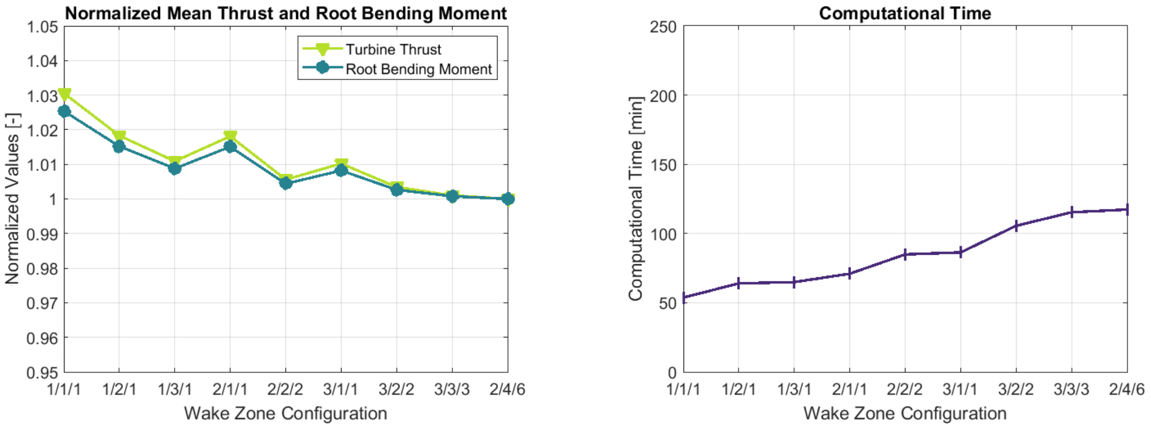

(a) Normalized mean thrust and mean root bending moment.

(b) Computational time.

Figure 3.6: Comparison of different wake zone configurations.

3.5. Numerical Set-Up

There are additional variables to be considered for coupled aero-servo-hydro-elastic simulations. The general parameters are found in Table 3.4. It was chosen to simulate 900 seconds of which the first 300 seconds are discarded to exclude initial transients. Furthermore, both the wind and wave headings are set to zero degrees. Consequently, any potential misalignment between wind and waves is excluded from this research. To facilitate a comparison between different DLCs, the random turbulence and wave seed are kept the same across all simulations.

Parameter	**Value**	**Units**
Simulation time	900	[s]
Time step	0.05	[s]
Azimuthal degree	1.5	[°]
Spectral model	IECKAI	
Dynamic stall model	Øye	
Shear exponent α	0.2	[-]
Roughness length z	0.01	[-]
Wind headings	0	[°]
Grid resolution	40	[points]
Grid width	274	[m]
Grid height	266	[m]
Turbulence seed	2097196	[-]
Wave headings	0	[°]
Wave seed	65665	[-]

Table 3.4: Numerical simulation settings.

4

Results

This chapter presents and discusses the results from the simulations with each section corresponding to a specific output parameter. Section 4.1 covers power output, Section 4.2 discusses torque, thrust is addressed in Section 4.3, root bending moment in Section 4.4, tip deflection in Section 4.5, and angle of attack in Section 4.6. Additionally, Section 4.7 includes a comparison with a bottom-fixed turbine to explore wave influences. From this chapter onward LLFVW is abbreviated to FVW. Appendix A provides hub height wind speed plots for each DLC to highlight the similarity between BEM and FVW simulations.

4.1. Power

The primary function of a wind turbine is to convert wind energy into electrical power. The power output directly reflects the efficiency and effectiveness of this conversion process. Comparing the power predicted by BEM and FVW methods provides insight into how well each method models the actual energy generation capabilities of the turbine. The power and thrust curves of the reference turbine are shown in Figure 4.1.

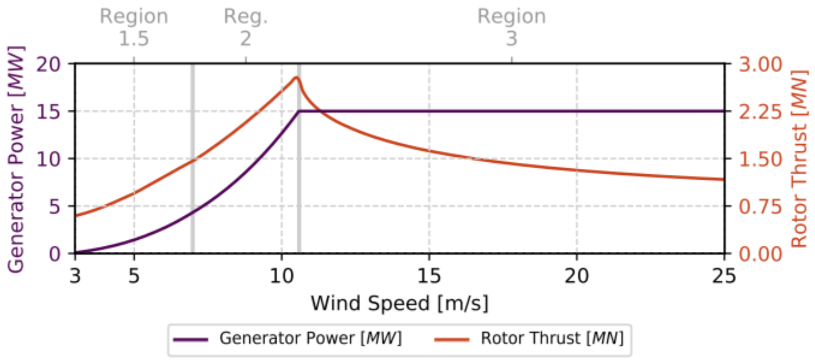

Figure 4.1: The power and thrust curve [55].

The three control regions are divided into:

1. **3 m/s $\leq$ U $\leq$ 6.98 m/s: minimum rotor speed.** The generator torque is controlled to maintain the turbine at its minimum rotor speed of 5 rpm.
2. **6.98 m/s $\leq$ U $\leq$ 10.59 m/s: optimal TSR.** In this range, a controller on the generator torque ensures the rotor speed matches the turbine's optimal Tip Speed Ratio (TSR) for efficient operation. A blade pitch setting of 0° is used when operating at the design TSR.
3. **10.59 m/s $\leq$ U $\leq$ 25 m/s: rated torque.** In above-rated wind speeds, the rotor speed is regulated by a PI controller on the blade pitch angle to maintain the rated speed of 7.55 rpm. For floating turbines, constant generator torque often replaces the constant-power setting.

The mean power output of the simulations are shown in Table 4.1, organized by mean hub height wind speed. When compared to the power curve, the power output at specific mean wind speeds demonstrates close alignment as can be seen in Figure 4.2. For above-rated wind speeds, the mean values approach the turbine's maximum capacity of 15 MW. For below rated conditions, the mean power output fluctuates the most between DLC 1.1 and 1.6 using FVW.

Additionally, the percentage differences are provided relative to the FVW simulations, offering a comparative assessment of the results. Noticeable is that the percentage difference is largest for a mean wind speed of 4 m/s, especially for DLC 1.6. At a wind speed of 18 m/s, the difference is smallest, which can be attributed to the conditions being far above the rated wind speed, where the turbine reaches its maximum capacity, limiting further variations in output.

HH mean wind speed	**DLC**	**10-minute Mean Power Output [kW]**		**Difference**
		FVW	**BEM**	
4 m/s	1.1	714.2	623.2	-12.8 %
	1.6	550.4	664.4	20.7 %
8 m/s	1.1	6677.3	6653.3	-0.4 %
	1.3	6910.9	7111.3	2.9 %
	1.6	6701.2	6719.1	0.3 %
10 m/s	1.1	11783.3	11673.8	-0.9 %
	1.3	11605.7	11543.8	-0.5 %
	1.6	11768.2	11658.0	-0.9 %
18 m/s	1.1	14991.4	14989.0	-0.02 %
	1.3	14965.5	14963.8	-0.01 %
	1.6	14992.5	14995.7	0.02 %
38 m/s	6.3	14735.9	14662.6	-0.5 %

Table 4.1: Mean power output for different wind speeds using FVW and BEM methods.

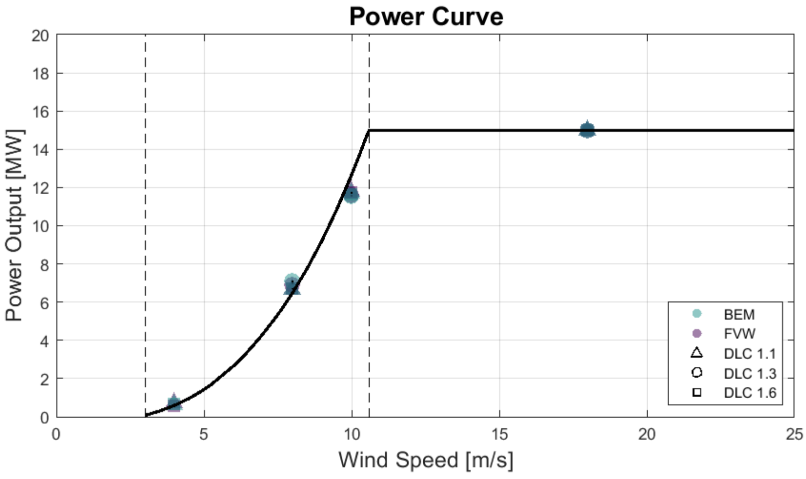

Figure 4.2: The power curve with mean power output per DLC.

The differences in power output between the two computational codes are given in Figure 4.3 for every DLC. Here the output of BEM is subtracted from the output of FVW. This means when the line is above zero, FVW predicts larger values and vice versa. Unfortunately, the simulation for DLC 1.3 using FVW with a mean wind speed of 4 m/s encountered issues and could not be completed, resulting in its omission from the plots. The likely cause of the computational errors was the combination of extreme turbulence conditions and low wind speed resulting in a substantial amount of vortex elements. Since the convergence study was based on a mean wind speed of 8 m/s under normal turbulence, it is possible that different wake settings are required for simulations involving lower wind speeds paired with extreme turbulence.

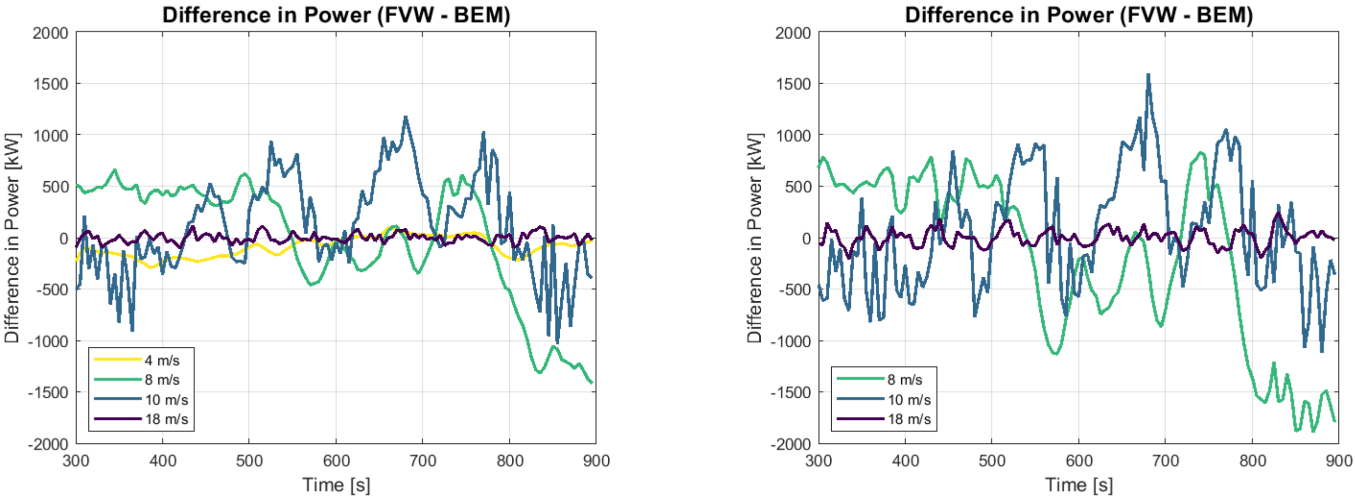

(a) Power difference DLC 1.1

(b) Power difference DLC 1.3

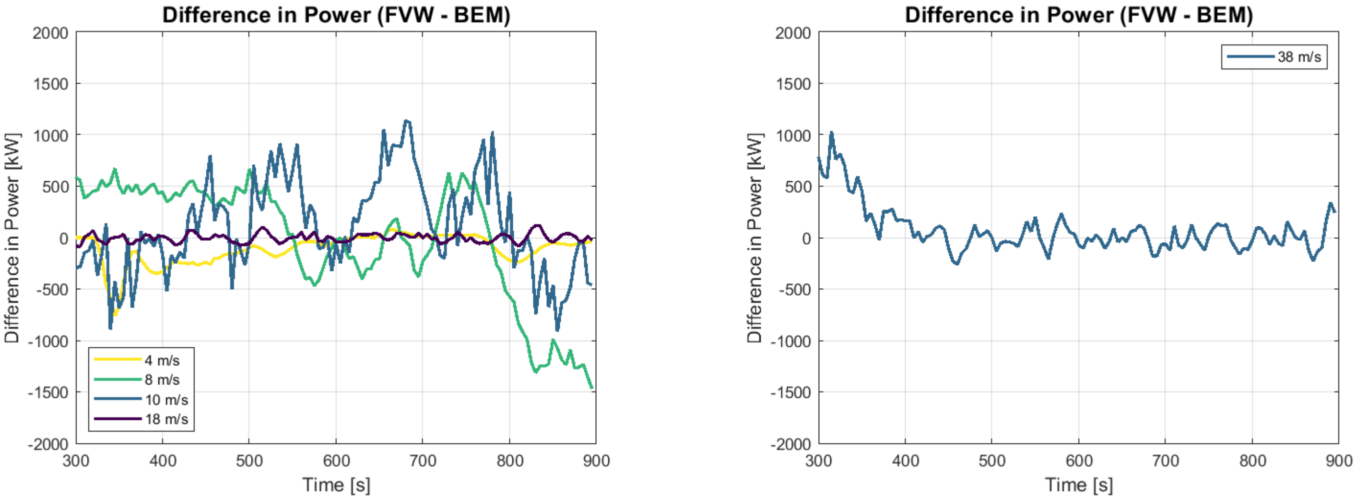

(c) Power difference DLC 1.6

(d) Power difference DLC 6.3

Figure 4.3: Power differences for the DLCs.

Figure 4.3a presents the differences in power production for DLC 1.1 for the simulated wind speeds. It is evident that the discrepancies are minimal for mean wind speeds of 4 m/s and 18 m/s, as the plots remain close to zero. However, for mean wind speeds of 8 m/s and 10 m/s, which approach rated conditions, the differences are more pronounced. For example for 8 m/s, the range is between 500 kW and -1500 kW and for 10 m/s between 1000 kW to -1000 kW. The largest difference occurs at 899.35 seconds for 8 m/s, here BEM predicts a power output of 11519 kW and FVW 10037.1 kW.

The time series of the difference in power for DLC 1.3 is plotted in Figure 4.3b. The difference in power production between methods is lowest for the highest wind speed of 18 m/s, while the around rated wind speeds show greater fluctuation in difference between BEM and FVW. The largest difference occurs at a wind speed of 8 m/s and reaches almost -2000 kW, the negative meaning that power output computed by BEM is higher than for FVW.

Figure 4.3c illustrates the time series of the power difference between BEM and FVW for DLC 1.6. The differences at wind speeds of 4 m/s and 18 m/s are relatively minor. Conversely, at wind speeds of 8 m/s and 10 m/s, the differences are more pronounced, exhibiting a broader range and greater fluctuation. For example, the range for 10 m/s varies between around -1000 to 1000 kW and the range for 8 m/s fluctuates between 500 to -1500 kW.

Figure 4.3d shows the difference in power output between BEM and FVW for DLC 6.3. The plot shows how the difference converges around zero after 400 seconds. Between 300 and 400 seconds BEM predicts a smaller power output than FVW. After that, the difference varies between -200 and 200 kW. It is worth noting that, under real-world conditions, the turbine would be parked due to the high wind speeds, so no power would be generated in this situation.

Discussion
From the figures illustrating the difference in power output between BEM and FVW a general trend can be observed between DLCs. The difference between methods is the least pronounced for the below and above rated wind speeds of 4 m/s and 18 m/s. For 8 m/s and 10 m/s, the around rated wind speeds, the power output between the methods fluctuates the most. Differences in how the methods account for factors such as turbulence, wake effects, and blade aerodynamic performance could lead to greater variations in predicted power output at these critical operational points. This fluctuation may stem from the turbine's controller dynamics being particularly sensitive during transitions between below-rated and above-rated conditions which are captured differently by BEM and FVW, while at 18 m/s, the turbine operates at maximum capacity with no changes in regulation.

A comparison between the DLCs highlights differences between BEM and FVW for turbulence and wave dynamics. In DLC 1.1 and DLC 1.3, which feature different turbulence models, the output trends remain similar, but the range increases when the extreme turbulence model is used in DLC 1.3. This holds for 8 m/s and 10 m/s mean wind speeds, while for 18 m/s the difference remains close to zero. When comparing DLC 1.1 with DLC 1.6, which incorporates elevated wave dynamics, the output differences between BEM and FVW are minimal, indicating that wave dynamics do not significantly affect the comparison between these methods in this case. For all wind speeds the trends and ranges remain the same.

4.2. Torque

In FOWTs, torque is crucial for understanding and managing the dynamic loads and stresses experienced by the rotor, platform, and mooring system. Accurate torque predictions ensure the structural integrity of the platform, optimize control strategies, and contribute to the overall efficiency and reliability of the floating wind turbine system. The torque regulation trajectory together with the mean torque output for the simulations are given in Figure 4.4. The results show close alignment with the torque trajectory for BEM as well as FVW. It can be seen that that the torque is limited to 20 MNm above the rated wind speed.

The 10-minute mean torque for all simulations are presented in Table 4.2. The results align well with the torque curve. For above rated wind speeds of 18 and 38 m/s, the torque approaches but stays just below 20 MNm. At around rated wind speeds of 8 and 10 m/s, the mean torques are approximately 11.5 and 16.3 MNm, respectively, as anticipated in control region 2. Similarly, for the below rated wind speed of 4 m/s, the mean torque is around 1.2 MNm, which is consistent with the torque curve. The difference in percentage is given relative to the FVW output. For 18 m/s the difference is negligible when the turbine operates at maximum torque. The largest difference occurs at 4 m/s, where for DLC 1.6 BEM has a mean torque that is 20.7% higher than FVW.

HH mean wind speed	DLC	10-minute Mean Torque [kNm]		Difference
		FVW	BEM	
4 m/s	1.1	1241.1	1422.7	14.6%
	1.6	1096.0	1322.9	20.7%
8 m/s	1.1	11459.9	11396.1	-0.6%
	1.3	11436.3	11421.5	-0.1%
	1.6	11505.3	11441.1	-0.6%
10 m/s	1.1	16420.0	16293.6	-0.8%
	1.3	16225.7	16110.1	-0.7%
	1.6	16418.5	16294.9	-0.8%
18 m/s	1.1	19786.7	19786.5	-0.001%
	1.3	19770.4	19767.5	-0.02%
	1.6	19782.6	19783.1	0.003%
38 m/s	6.3	19631.1	19557.1	-0.4%

Table 4.2: Mean torque for different wind speeds using FVW and BEM methods.

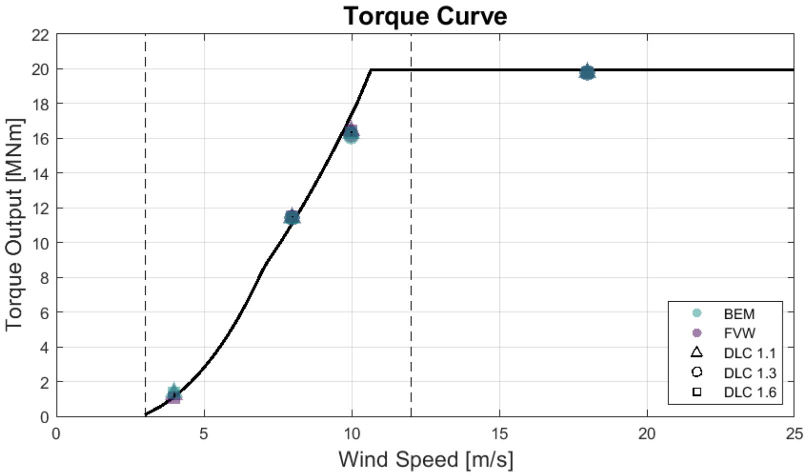

Figure 4.4: The torque curve with mean torque output per DLC.

The difference in torque as modelled by BEM and FVW for the DLCs are given in Figure 4.5. The values for BEM are subtracted from the FVW values, meaning when the line is positive BEM provides higher values than FVW and vice versa.

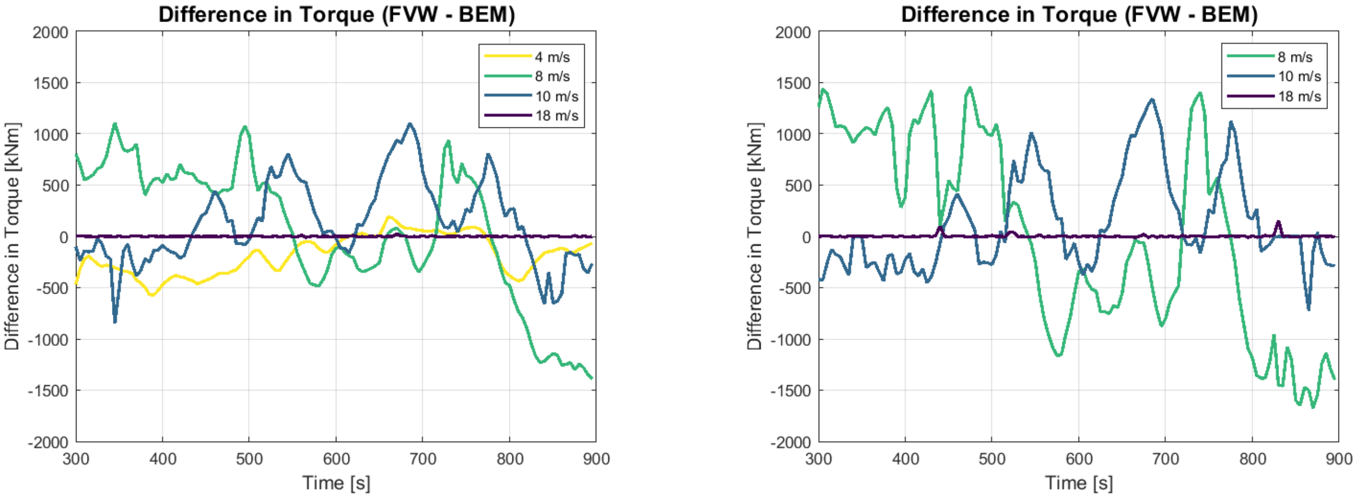

(a) Torque difference DLC 1.1.

(b) Torque difference DLC 1.3.

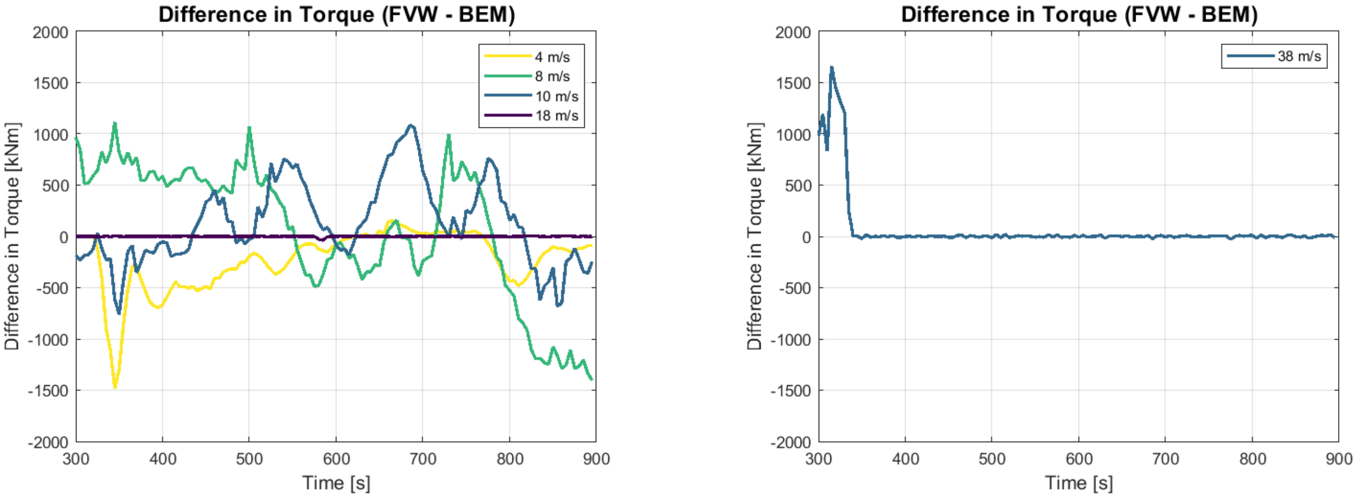

(c) Torque difference DLC 1.6.

(d) Torque difference DLC 6.3.

Figure 4.5: Torque differences for the DLCs.

The difference in torque for DLC 1.1 is shown in Figure 4.5a. Notably, the difference in torque at a mean wind speed of 18 m/s is negligible, approaching zero. In contrast, at a mean wind speed of 4 m/s, the difference is predominantly negative, suggesting that the torque values predicted by BEM are generally higher than those predicted by FVW. Additionally, the variations in torque for wind speeds of 8 m/s and 10 m/s are more erratic, reflecting greater fluctuations in the torque predictions between the two methods at these near-rated wind speeds.

The time series of the difference in torque for DLC 1.3 is plotted in Figure 4.5b. The difference in torque between methods is lowest for the highest wind speed of 18 m/s, while the around rated wind speeds show greater fluctuation in difference between BEM and FVW. The largest differences occur at a wind speed of 8 m/s where the difference between BEM and FVW varies between 1500 and -1500 kNm.

The difference in torque for DLC 1.6 between FVW and BEM is shown in Figure 4.5c. As observed in other load cases, the torque dissimilarity at a mean wind speed of 18 m/s is minimal, approaching zero. The difference at 4 m/s is predominantly below zero, indicating that BEM yields higher values compared to FVW. The torque difference of wind speeds around rated conditions, 8 and 10 m/s, shows a similar fluctuating trend as before.

The torque difference for DLC 6.3 is presented in Figure 4.5d. It can be seen that the difference between BEM and FVW approaches zero after 400 seconds. At the start of the simulation, there is a notable discrepancy in the torque values predicted by BEM and FVW, with the difference reaching approximately 1600 kNm. This initial overshoot indicates that the two methods are capturing different dynamics in the early phase of the simulation, possibly due to the transient response of the system or differences in how each method handles the initialization and early aerodynamic interactions.

Discussion

The figures illustrating the torque differences between BEM and FVW show similar results between DLCs. Across all DLCs the difference in torque output for a mean wind speed of 18 m/s was nearly close to zero. For a mean wind speed of 4 m/s, the torque difference indicated that BEM produced higher values compared to FVW, as the plots were mostly below zero. Again for the wind speeds around rated conditions both negative and positive values were obtained showcasing a very fluctuating pattern. This increased variability highlights the sensitivity of the torque predictions to changes in wind speed around the rated operating conditions.

These observed trends are likely related to the dynamics of the turbine's control system. At a mean wind speed of 18 m/s, the turbine operates in the above rated wind speed region, where the control system maintains a constant maximum torque. This seems to be captured well by BEM and FVW. At 4 m/s the controller regulates the torque to maintain the minimum rotor speed of 5 rpm. In Appendix C the time series of the torque for every wind speed and DLC are given. Additionally, in Appendix B the pitch angle is given for all DLCs and wind speeds.

When comparing the different DLCs, similar trends are noticeable across the datasets. The main distinction between DLC 1.1 and DLC 1.3 is observed at wind speeds of 8 and 10 m/s, where a greater spread occurs, likely due to the extreme turbulence in DLC 1.3. For DLC 1.1 and DLC 1.6, the time series appear almost identical, except for a significant downward peak around 340 seconds at 4 m/s. This anomaly likely stems from a QBlade modelling error.

4.3. Thrust

Thrust is the force exerted by the wind on the rotor blades in the direction of the wind. Accurate thrust predictions are essential for designing the floating platform and mooring system, ensuring structural integrity, optimizing performance, and developing effective control strategies. The thrust curve for the reference turbine is given in Figure 4.1.

In Table 4.3 the mean thrust for the simulations is given, sorted by mean hub height wind speed. Comparing these values with the thrust curve reveals that the 10-minute averages closely align with expected performance across different wind speeds. The largest difference between methods occurs for DLC 6.3 when BEM finds a mean thrust that is 18.7% lower than FVW. The thrust force is largest at a mean wind speed of 10 m/s which is closest to the rated wind speed of 10.59 m/s. For 4 m/s, the mean thrust computed with BEM is larger for both DLCs than with FVW. The mean values are plotted next to the reference thrust curve in Figure 4.6 where it can be seen that the thrust output is overall lower in comparison with the reference, yet the mean thrust output of BEM and FVW closely align.

HH mean speed wind	**DLC**	**10-minute Mean Thrust [kN]**		**Difference**
		FVW	**BEM**	
4 m/s	1.1	277.9	304.3	9.5%
	1.6	247.2	272.2	10.1%
8 m/s	1.1	1273.4	1257.8	-1.2%
	1.3	1251.2	1223.6	-2.2%
	1.6	1274.9	1258.2	-1.3%
10 m/s	1.1	1668.1	1637.9	-1.8%
	1.3	1584.6	1538.4	-2.9%
	1.6	1658.0	1627.8	-1.8%
18 m/s	1.1	1056.9	1031.0	-2.5%
	1.3	1042.7	1004.5	-3.7%
	1.6	1052.9	1026.9	-2.5%
38 m/s	6.3	342.2	278.4	-18.7%

Table 4.3: Mean thrust for different wind speeds using FVW and BEM methods.

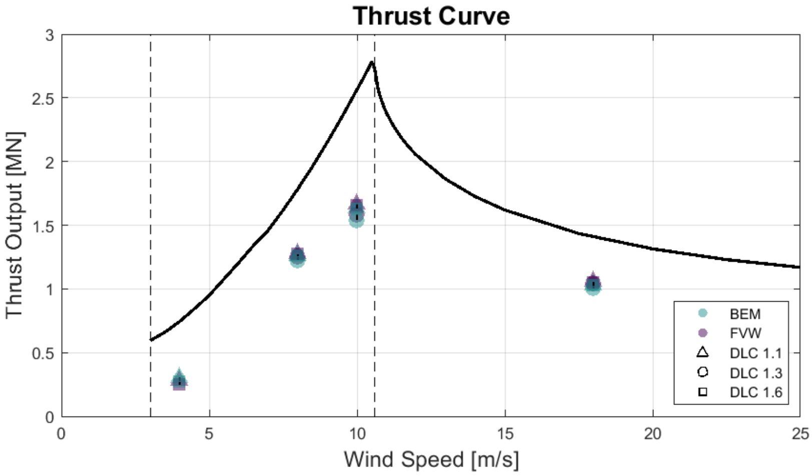

Figure 4.6: The thrust curve with mean thrust output per DLC.

The difference in thrust output for FVW and BEM simulations are plotted in Figure 4.7. Again, the output from BEM is subtracted from the FVW output.

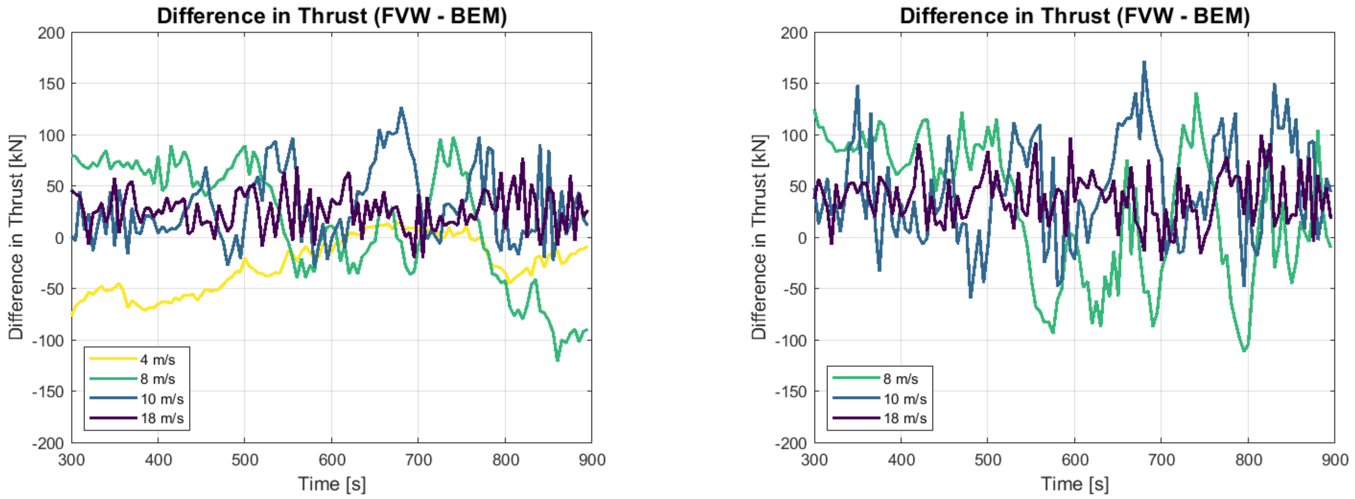

(a) Thrust difference DLC 1.1

(b) Thrust difference DLC 1.3

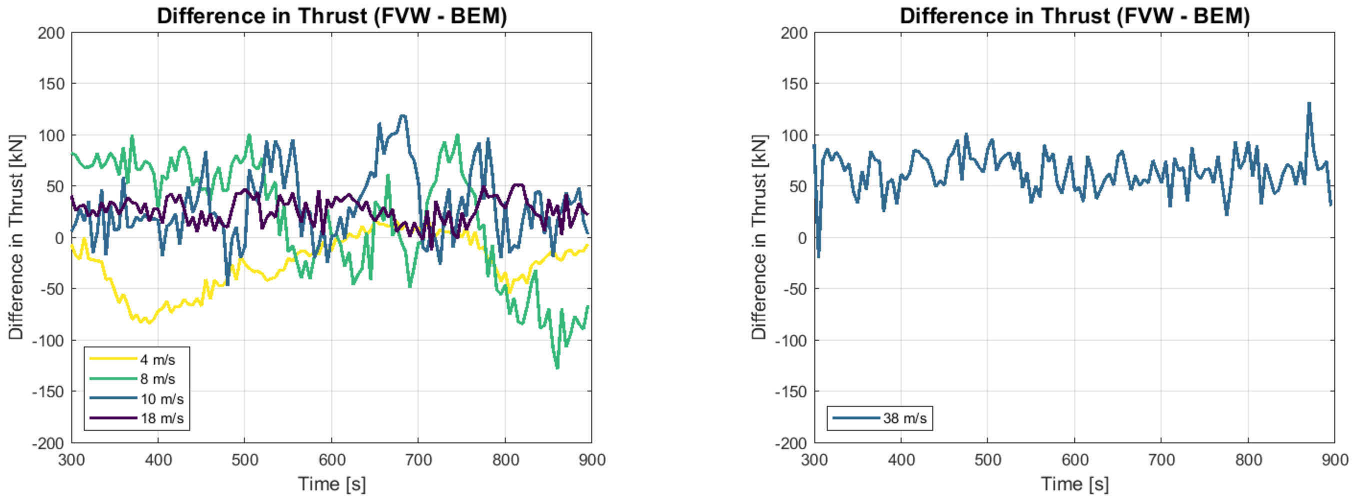

(c) Thrust difference DLC 1.6

(d) Thrust difference DLC 6.3

Figure 4.7: Difference in thrust for the DLCs.

The difference in thrust for DLC 1.1 between the two codes is plotted in Figure 4.7a. At the lowest wind speed of 4 m/s, the values are mostly consistent negative, in contrast to the predominantly positive values observed at higher wind speeds of 10 and 18 m/s. The thrust difference for 8 m/s has the widest range spanning from -100 kN to 100 kN.

The thrust difference for DLC 1.3 is depicted in Figure 4.7b. It is evident that at 18 m/s, the values are predominantly positive, indicating that the FVW values exceed those of BEM. The variation in difference between BEM and FVW are more pronounced at wind speeds of 8 and 10 m/s. Here the maximum difference is at 8 m/s and over 100 kN at around 800 seconds, where FVW predicts a higher thrust.

Figure 4.7c illustrates the difference in thrust as seen by BEM and FVW for DLC 1.6. The below rated wind speed of 4 m/s shows a negative line indicating higher thrust found by BEM compared to FVW. For 18 m/s the situation is reversed showing predominantly positive values ranging between 0 and -50 kN. At 8 and 10 m/s the difference in thrust shows considerable variability, alternating between positive and negative values. This indicates that the difference between the two methods is less consistent and fluctuates significantly as the wind speed approaches rated conditions.

Figure 4.7d illustrates the difference in thrust for DLC 6.3. The graph demonstrates that the thrust values predicted by BEM are consistently lower than those predicted by FVW, as indicated by the line being predominantly above zero. This suggests that the BEM method tends to underestimate the thrust compared to FVW under the specific conditions of DLC 6.3 which include a yaw angle of 20°.

Discussion

Examining thrust is particularly interesting because it does not involve any controller dynamics. A few consistent trends along the DLCs regarding thrust occurred. The first one is that the thrust difference for the highest wind speed of 18 m/s was above zero for all DLCs, indicating that the BEM values were lower than the FVW values. In contrast, for a wind speed of 4 m/s the values were consistently negative across DLCs, meaning that BEM predicted higher values than FVW. Once more, the 8 m/s and 10 m/s showed the largest discrepancies between the methods. In general, the mean thrust values from BEM were lower than those from FVW, except for wind speeds below the rated threshold. This difference might be due to the wake settings of FVW, which may not be well-suited for lower wind speeds. Thrust is an interesting output to look at, because no controller dynamics are involved.

To discuss the influence of turbulence on thrust outputs between BEM and FVW, a comparison between DLC 1.1 and DLC 1.3 is made. What can be noticed is that the trend is similar, but the range is broadened. This is especially true for the 8 m/s simulation. To evaluate the influence of wave elevation, DLC 1.1 is compared with DLC 1.6. As was the case for the previous output parameters, it can be stated that the waves have very little influence on the differences between BEM and FVW simulations.

4.4. Root Bending Moment

The root bending moment is the bending force experienced at the base of the wind turbine blades where they connect to the hub or the rotor shaft. In FOWTs, the root bending moment is a critical parameter for assessing the structural integrity of the blades, optimizing design, performing fatigue and lifespan analysis, and ensuring safe and reliable operation. Accurate predictions of root bending moments are essential for designing the turbine and platform to handle dynamic loads, planning maintenance, and enhancing the overall safety and performance of the system.

For every DLC the maximum out-of-plane (OOP) root bending moment is presented in Figure 4.8, as well as the standard deviation. The standard deviation indicates how much the values deviate from the mean, thus providing a comprehensive understanding of the performance characteristics under varying loading conditions.

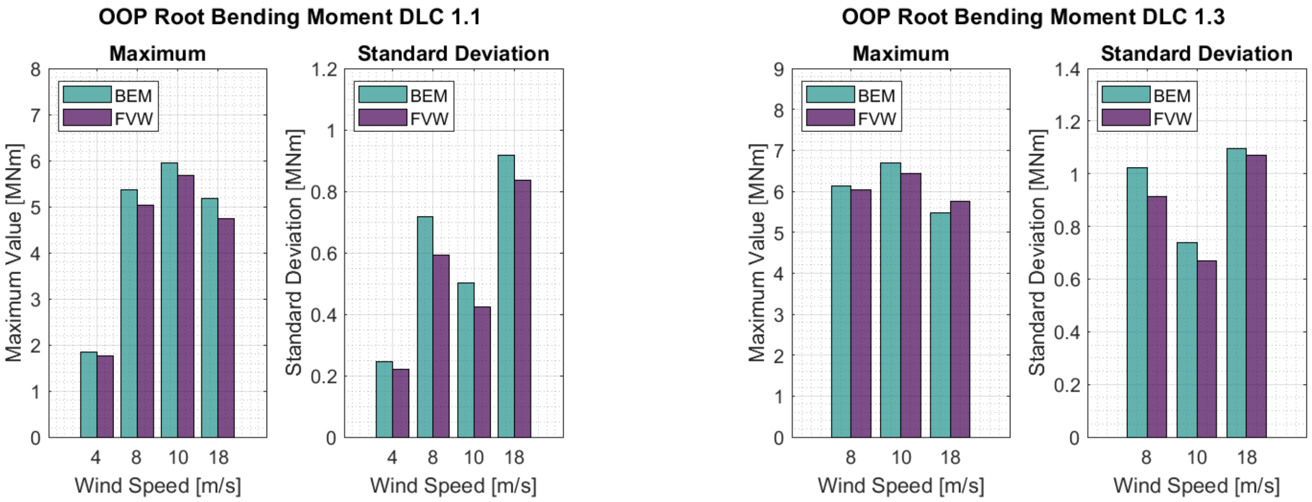

(a) OOP Root bending moment DLC 1.1

(b) OOP Root bending moment DLC 1.3

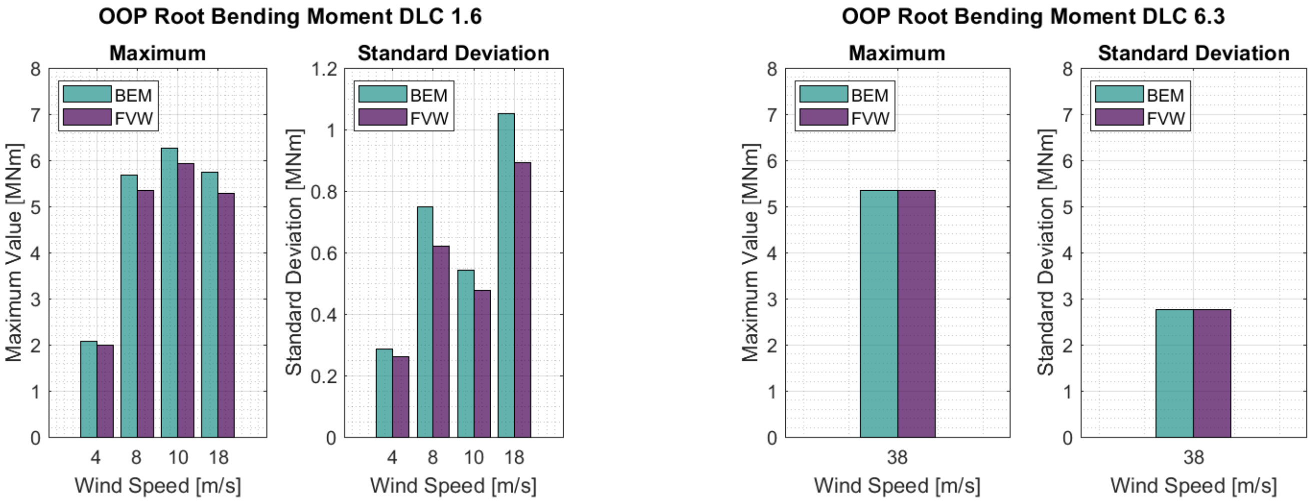

(c) OOP Root bending moment DLC 1.6

(d) OOP Root bending moment DLC 6.3

Figure 4.8: OOP root bending moments for the DLCs.

The variations in out-of-plane root bending moment of blade 1 for DLC 1.1 are presented in Figure 4.8a. The figure shows that both the maximum value and the standard deviation are higher computed by BEM compared to FVW. Notably, at the lowest wind speed of 4 m/s, the differences are minimal. However, for the other wind speeds the difference between the methods is very similar. Regarding standard deviation, the difference between BEM and FVW is most pronounced at the 8 m/s wind speed, followed by 18 m/s and 10 m/s.

Figure 4.8b shows the maximum root bending moment and standard deviation for DLC 1.3. The differences between BEM and FVW are relatively small, especially when looking at the maximum value. However, a notable observation is that the maximum at a mean wind speed of 18 m/s is higher for FVW compared to BEM in contrast to the other wind speeds. Additionally, the standard deviation of the OOP root bending moment displays more pronounced differences at a wind speed of 8 m/s compared to other wind speeds with BEM predicting a higher value.

In Figure 4.8c the maximum root bending moment and standard deviation for DLC 1.6 is given. It is evident that BEM consistently predicts higher maximum root bending moments than FVW across all wind speeds. Additionally, BEM shows greater variability in the standard deviation compared to FVW, with a significant outlier at 18 m/s and substantial variation also observed at 8 m/s.

When comparing the root bending moment between the methods for DLC 6.3, Figure 4.8d shows that the difference is minimal. Both the maximum value and standard deviation given by BEM and FVW are close to equal.

Discussion

In general, the findings demonstrate that BEM yields greater values for the root bending moment compared to FVW. The largest differences were spotted between BEM and FVW for DLC 1.6. Here, BEM consistently predicted higher values for both the maximum and standard deviation. In contrast, for DLC 1.3 the differences between codes were least significant. The higher values of BEM for OOP blade root moment are in line with other findings, such as from Perez-Becker [27] and Boorsma [41]. Both studies further analysed the fatigue and extreme loads which where overestimated by BEM.

The increased wave elevation in DLC 1.6 at 18 m/s affects the standard deviation of the BEM results compared to DLC 1.1, with the former exhibiting a greater standard deviation than in the lower wave scenario. In contrast, the results for the FVW method in both DLC 1.1 and 1.6 appear to be similar. The standard deviation differences between BEM and FVW for DLC 1.3 were notably smaller than those for DLC 1.1, particularly at wind speeds of 8 and 18 m/s, where the results were much more closely aligned.

4.5. Tip Deflection

Tip deflection refers to the bending or displacement of the blade tip due to aerodynamic forces, gravity, and structural loads. In FOWTs, tip deflection is a key parameter for ensuring proper blade design, maintaining aerodynamic performance, and managing loads and structural interactions. Accurate prediction and monitoring of tip deflection are essential for optimizing performance, performing fatigue analysis, ensuring safety, and planning maintenance. The maximum OOP tip deflection and standard deviation for all DLCs are given in Figure 4.9.

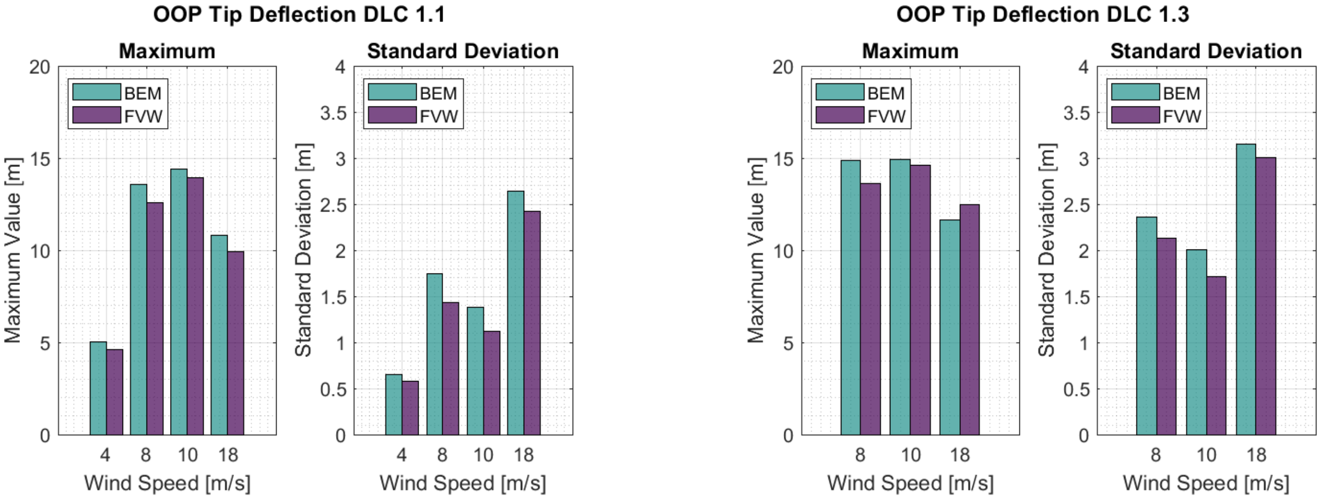

(a) OOP tip deflection DLC 1.1 **(b)** OOP Tip deflection DLC 1.3

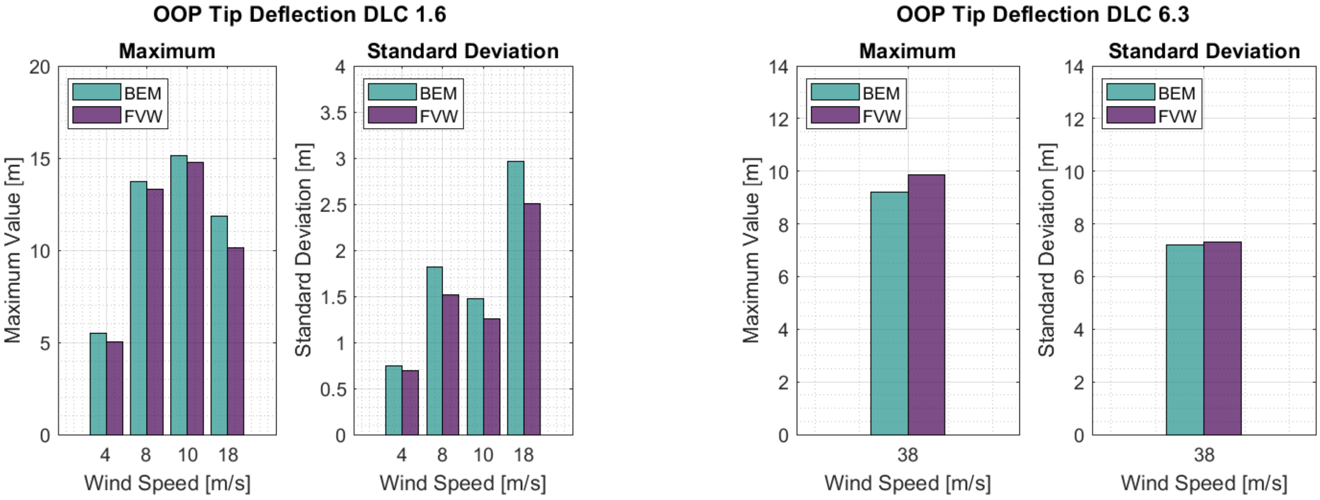

(c) OOP Tip deflection DLC 1.6 **(d)** OOP Tip deflection DLC 6.3

Figure 4.9: OOP tip deflections for the DLCs.

The results of out-of-plane tip deflection for DLC 1.1 are shown in Figure 4.9a. Similarly to the root bending moment, the values for maximum and standard deviation are higher for BEM than for FVW. At the lowest wind speed of 4 m/s the differences are again the smallest. Next to that, the differences are most pronounced for 8 m/s followed by 10 m/s and 18 m/s.

In Figure 4.9b the maximum tip deflection and standard deviation are illustrated for this DLC. There is no trend where one method consistently predicts higher maximum values than the other. However, a notable difference lies in the variability of the results: the BEM method consistently shows higher standard deviation values compared to the FVW method. This suggests that the BEM method predicts a wider range of deflection magnitudes, indicating a greater sensitivity to the variations in the input conditions or a potential overestimation of deflections under certain conditions.

Figure 4.9c shows the maximum tip deflection and standard deviation for DLC 1.6. A similar pattern is occurring as for the root bending moment with BEM giving higher values for maximum and standard deviation than FVW. Recurrently, the most significant difference is the standard deviation at 18 m/s where the standard deviation of tip deflection predicted by BEM is nearly 0.5 meters higher than that predicted by FVW.

The maximum tip deflection and standard deviation for both codes for DLC 6.3 is shown in Figure 4.9d. In contrast to other DLCs, for both the maximum and standard deviation FVW provides higher values. The standard deviation for this DLC is significantly greater than that observed in the other DLCs which can be attributed to the high wind speed.

Discussion

The results for the tip deflection align closely with the findings for the root bending moment across various DLCs. This correlation is not surprising, as the bending moment at the root of the blade is a primary determinant of the overall structural response, including the tip deflection. Therefore, any variations observed in the root bending moments due to differences in the modelling approaches, BEM and FVW, are likely to be reflected in the tip deflection measurements.

The overall trend for tip deflection is that BEM presents higher values than FVW, with exception of the 18 m/s simulation for DLC 1.3 and the simulation for DLC 6.3. BEM's tendency to predict greater tip deflection could lead to a design that overestimates structural stiffness, potentially resulting in an over-engineered turbine. This could mean unnecessary material use and higher costs without corresponding performance benefits. The FVW model, by offering more accurate predictions of wake dynamics, might provide more realistic feedback on the loads experienced by the blades, especially in dynamic offshore conditions.

4.6. Angle of Attack

In floating wind turbines, the angle of attack is a critical parameter for optimizing performance, preventing stall, and managing loads. Three points on the blade span are evaluated: at 0.30, 0.50 and 0.85 of the blade radius which is abbreviated to R. The airfoil used for this turbine is the FFA-W3 series, the same as for the DTU 10 MW reference turbine [62]. Table 4.4 gives the design and stall angles per airfoil.

Blade Section	**Airfoil**	α_{des} [°]	α_{stall} [°]
0.30R	FFA-W3-360	6.58	12
0.50R	FFA-W3-301	8	14
0.85R	FFA-W3-211	9.16	16

Table 4.4: Stall angles at different blade sections [63].

The primary motivation for comparing BEM and FVW methods in predicting the angle of attack lies in determining which method more accurately predicts the onset of dynamic stall. Dynamic stall occurs when airflow over the blade becomes separated due to rapidly changing angles of attack, leading to a significant drop in lift and an increase in drag. Early prediction of this phenomenon is crucial for turbine control and design, as it affects the aerodynamic performance and structural loads on the turbine blades [64].

FVW, with its explicit wake modelling, might capture unsteady aerodynamic effects better than BEM, which relies on steady-state assumptions. This comparison can help identify whether FVW offers an advantage by predicting dynamic stall at an earlier point than BEM, thus contributing to improved control strategies, particularly in turbulent or gusty wind conditions .

4.6.1. DLC 1.1

To compare the angle of attack between the two methods, box plots of the four wind speeds are presented in Figure 4.10. At three different blade spans the angle of attack is evaluated, at 0.30 (Fig.4.10a), 0.50 (Fig.4.10b) and 0.85 (Fig.4.10c) of the blade radius.

It can be seen that the discrepancy is smallest at the lowest wind speed of 4 m/s, here all aspects of the box plots are very similar. In contrast, the largest difference can be found at 18 m/s wind speed. There it can be seen that the spread is larger for BEM than for FVW, especially at 0.30R and 0.50R. The median of the angle of attack is mostly comparable between the methods. On exception at blade span 0.50R where for the wind speeds of 8, 10 and 18 m/s the median for FVW is higher than for BEM.

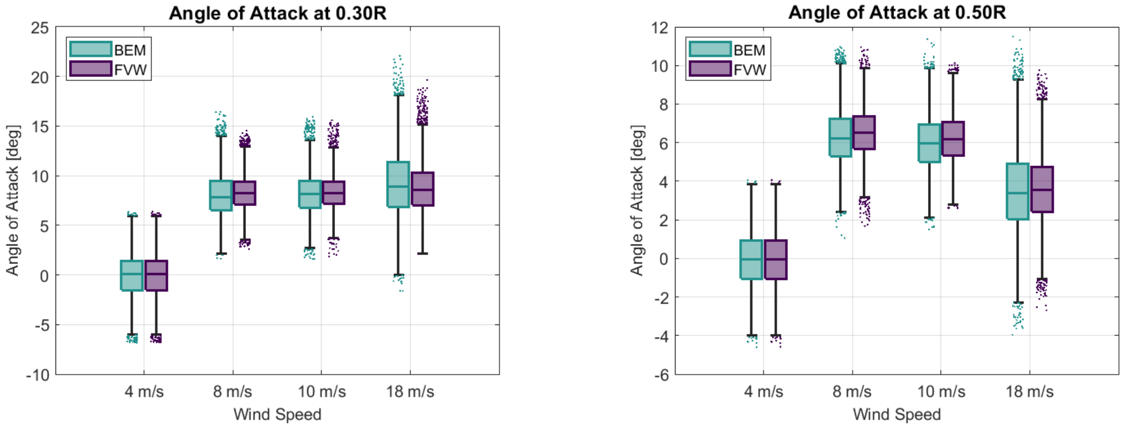

(a) AoA at blade span 0.30R.

(b) AoA at blade span 0.50R.

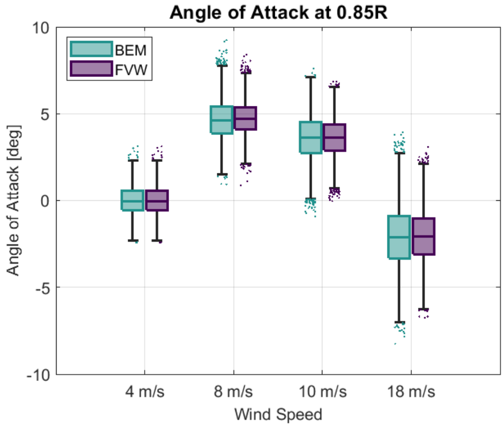

(c) AoA at blade span 0.85R.

Figure 4.10: AoA for different wind speeds of DLC 1.1 at different blade spans.

4.6.2. DLC 1.3

The box plots for the angle of attack for DLC 1.3 at different blade spans are presented in Figure 4.11. The data reveals that BEM consistently exhibits a wider spread in the angle of attack across all measured blade spans, indicating a greater variability in its predictions compared to FVW. At a blade span of 0.30R the differences are most pronounced, especially for 18 m/s. Here, the median angle of attack predicted by FVW is notably lower than that predicted by BEM, which is an outlier compared to the trends observed at other blade spans and wind speeds.

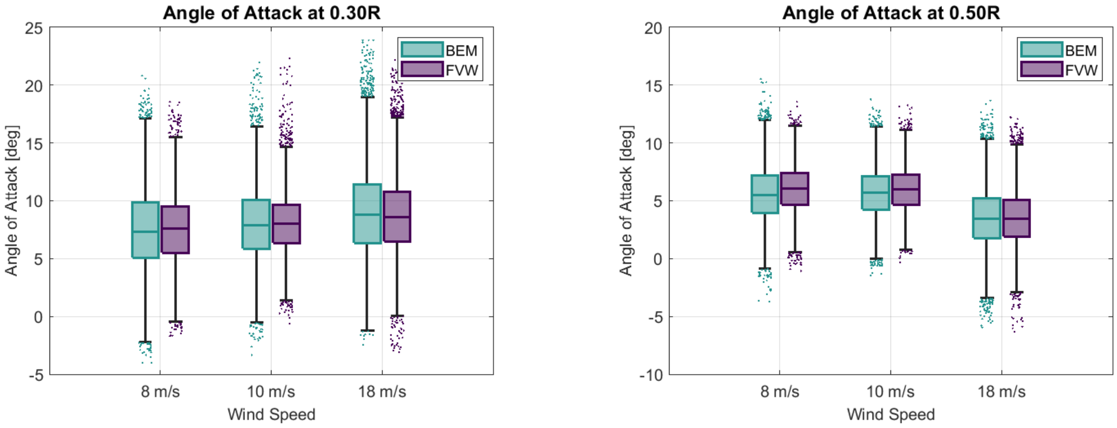

(a) AoA at blade span 0.30R.

(b) AoA at blade span 0.50R.

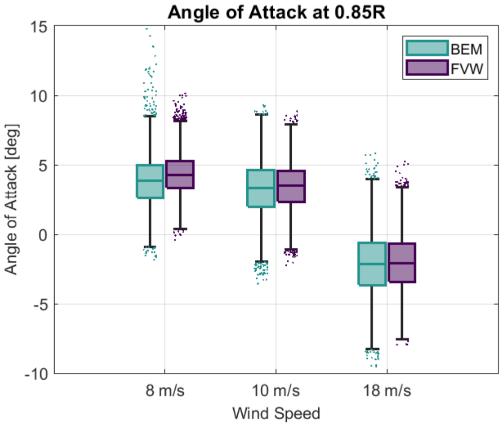

(c) AoA at blade span 0.85R.

Figure 4.11: AoA for different wind speeds of DLC 1.3 at different blade spans.

4.6.3. DLC 1.6

Figure 4.17 presents the box plots of angle of attack for DLC 1.6. Notably, there is a significant similarity between the BEM and FVW methods at the low wind speed of 4 m/s, indicating comparable performance under these conditions. However, as the wind speed increases, differences between the methods become more apparent. Specifically, BEM exhibits a greater variability in the angle of attack at higher wind speeds, with the most pronounced difference observed at 18 m/s.

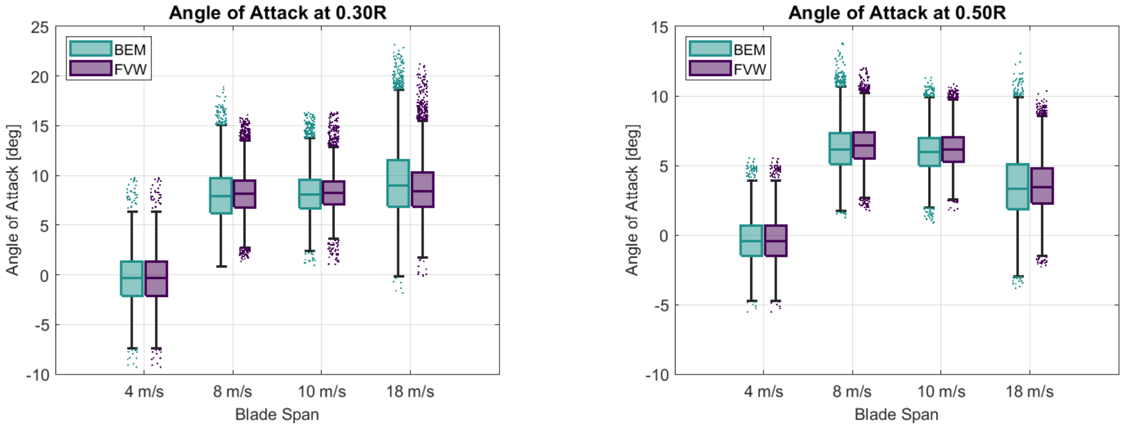

(a) AoA at blade span 0.30R.

(b) AoA at blade span 0.50R.

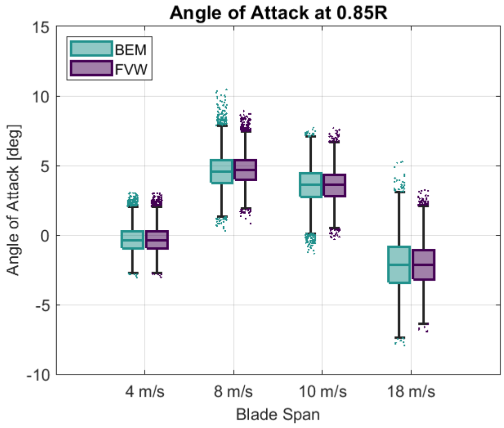

(c) AoA at blade span 0.85R.

Figure 4.12: AoA for different wind speeds of DLC 1.6 at different blade spans.

4.6.4. DLC 6.3

The box plots in Figure 4.13, depicting the angle of attack for DLC 6.3, show that BEM and FVW yield similar results. The medians are closely aligned, and the number of outliers is comparable between the two methods. Notably, at 0.85R, the number of outliers is significant for both methods.

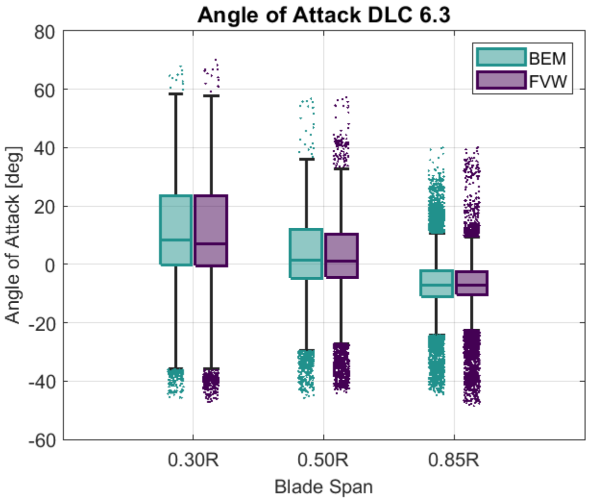

Figure 4.13: Angle of Attack DLC 6.3.

Discussion

Over all performed simulations it can be stated that BEM showed a greater spread in angle of attack than FVW. This was most pronounced for the highest wind speed of 18 m/s. This suggests that BEM may predict the onset of stall earlier than FVW, potentially leading to conservative assessments of turbine performance. Consequently, this could result in underestimations of the actual aerodynamic efficiency, as BEM might indicate stalling conditions when, in reality, the flow remains attached [64] [65].

When using FVW, the wake dynamics of a wind turbine are explicitly simulated, allowing for more accurate and detailed feedback on the interaction between the wake and the turbine blades. This explicit modelling captures the unsteady aerodynamic effects, such as vortex shedding and wake-induced forces, which affect blade performance. As a result, FVW provides a more precise representation of changes in blade aerodynamics compared to methods like BEM. This feedback between wake and blade aerodynamics could explain the narrower spread for FVW compared to BEM.

4.7. Floating & Bottom-Fixed Turbine

In order to investigate the influence of waves on the differences between BEM and FVW, a simulation with a bottom-fixed wind turbine is conducted. The reference turbine used for this is the IEA Wind 15-Megawatt Offshore Reference Wind Turbine as described in IEA Wind TCP Task 37 [55]. The floating turbine is the one previously used and described in Section 3.1. A difference between the floating version is in the controller region above rated wind conditions. For floating, the controller keeps the generator torque constant. For bottom-fixed, the power is held constant by adjusting the blade pitch angle to maintain the rated speed. The simulation was centered on a wind speed of 18 m/s in combination with the NTM, which aligns with the conditions of the highest significant wave height and peak wave period.

The time series of the power output is shown in Figure 4.14, with the FOWT in Figure 4.14a and the bottom-fixed in Figure 4.14b. For both plots the difference between BEM and FVW are minimal as the lines align almost completely. The main difference is in the power produced which is related to the controller conditions and is a difference between bottom-fixed and floating turbines.

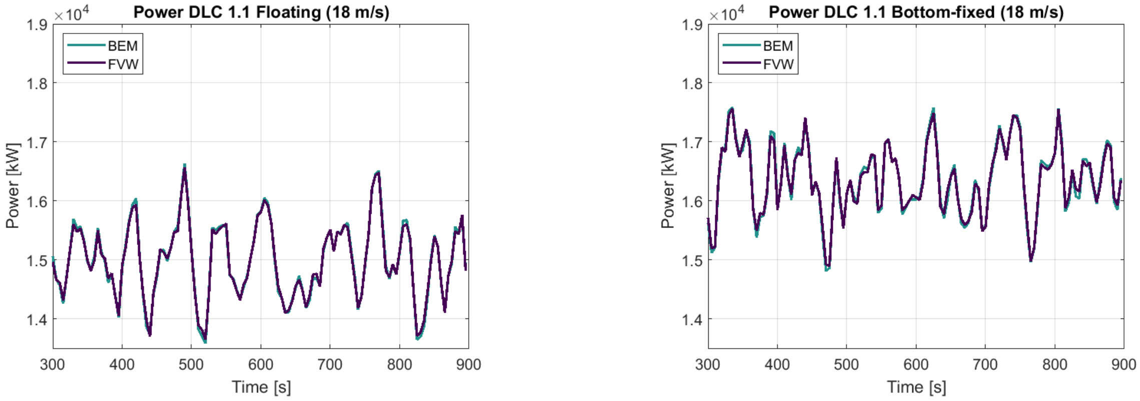

(a) Power output for floating turbine.

(b) Power output for bottom-fixed turbine.

Figure 4.14: Power for floating and bottom-fixed turbine.

The torque output for the floating and bottom-fixed wind turbine are shown in Figure 4.15. The difference between these plots can be attributed to the control strategy for above rated conditions. The FOWT controller keeps the torque constant, while the bottom-fixed controller keeps the power constant by adjusting the pitch angle. Overall the difference between BEM and FVW looks similar for the floating and bottom-fixed case.

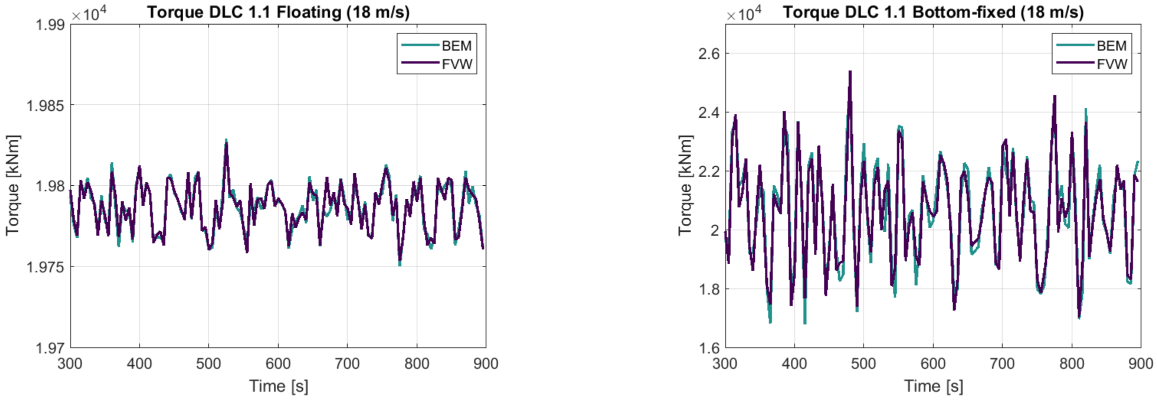

(a) Torque output for floating turbine.

(b) Torque for bottom-fixed turbine.

Figure 4.15: Torque for floating and bottom-fixed turbine.

The thrust is illustrated in Figure 4.16 with the FOWT in Figure 4.16a and the bottom-fixed turbine in Figure 4.16b. In both cases, the thrust values obtained using BEM exhibit lower values during the low peaks, which stands out when compared to the FVW results. This pattern is consistent across both turbine configurations, highlighting the tendency of BEM to underpredict thrust during certain phases of the simulation.

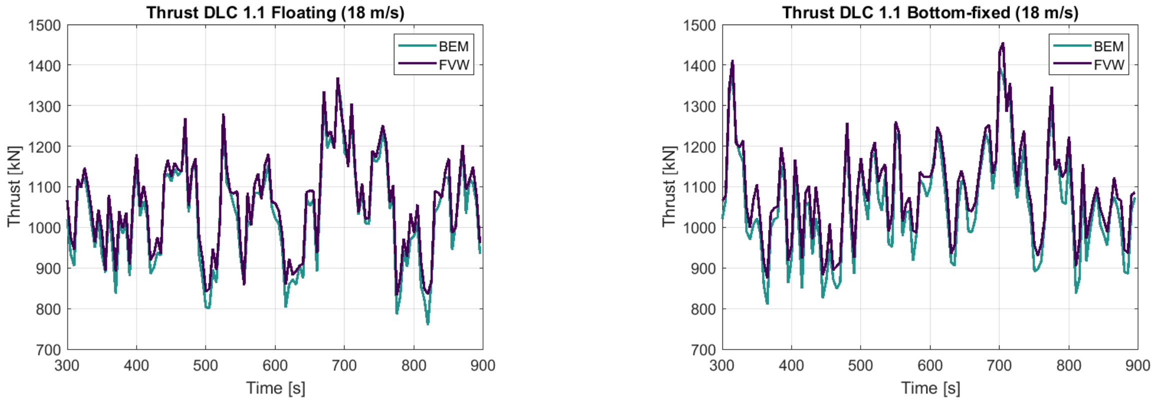

(a) Thrust output for floating turbine.

(b) Thrust for bottom-fixed turbine.

Figure 4.16: Thrust for floating and bottom-fixed turbine.

The angle of attack is evaluated at 0.30, 0.50 and 0.85 of the blade radius and presented in Figure 4.17a, Figure 4.17b and Figure 4.17c, respectively. At 0.30R, a notable difference between BEM and FVW is observed, with the floating turbine showing a larger discrepancy. The mean AoA from FVW is lower than that predicted by BEM. A similar trend is observed for the bottom-fixed turbine, but the difference is less pronounced compared to the floating turbine case. At 0.50R, the means of BEM and FVW compare better.

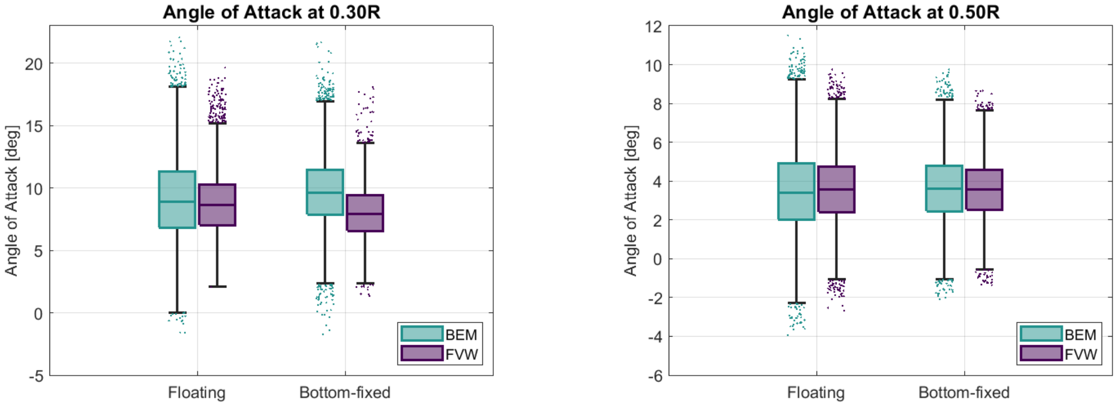

(a) AoA at blade span 0.30R.

(b) AoA at blade span 0.50R.

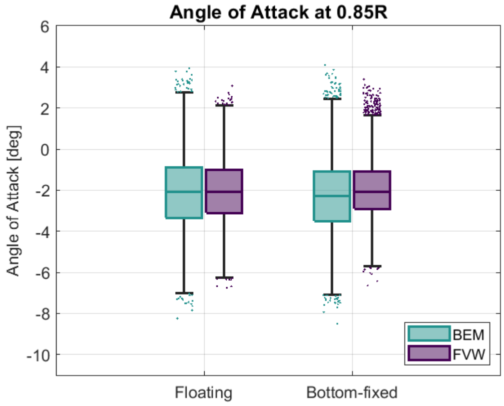

(c) AoA at blade span 0.85R.

Figure 4.17: AoA for different wind speeds of DLC 1.6 at different blade spans.

Discussion

Focusing solely on the differences between BEM and FVW for the floating and bottom-fixed turbine, the analysis suggests that the presence of waves does not significantly affect the disparity between the two methods. Despite the dynamics introduced by floating platforms, the variation between BEM and FVW remains consistent in both floating and bottom-fixed simulations. This implies that wave influence does not play a substantial role in altering the predictive differences between these aerodynamic models.

5

Conclusion

This chapter provides answers to the research questions and concludes the study.

In this thesis, 13 simulations were performed for each computational method, representing a range of wind and wave conditions to reflect the unsteady environment a FOWT may encounter. The goal was to compare BEM and FVW and determine for which met-ocean conditions the differences between them are most significant. The following sub-questions have been addressed:

What is the dependency on wind conditions?

The wind conditions simulated in this study include mean wind speeds of 4, 8, 10, and 18 m/s, covering below, around, and above-rated conditions. Two turbulence models, the normal turbulence model and the extreme turbulence model, were also used.

At 4 m/s (below rated), BEM and FVW produced similar results for power and torque, but BEM consistently predicted higher thrust. For root bending moments and tip deflections, both methods showed comparable results, and the angle of attack exhibited minimal differences. However, it is possible that the wake settings used for FVW, optimized for 8 m/s, were not ideal for this lower wind speed.

At around-rated wind speeds (8 and 10 m/s), the largest fluctuations between the methods were observed for power, torque and thrust. The results differed significantly, with BEM sometimes overestimating and sometimes underestimating power, torque, and thrust output compared to FVW. These differences are probably due to the increased sensitivity of the controller dynamics at the transition points between the control regions. The mean values were similar, with BEM's output being slightly lower than that of FVW. BEM predicted higher root bending moments and tip deflections, which could lead to overly conservative turbine designs. The angle of attack at these wind speeds showed a greater variability for BEM than for FVW.

For the above-rated wind speed of 18 m/s, BEM and FVW showed good alignment for power and torque predictions, likely due to the turbine being at its rated capacity, thus limiting further variations in controller regulation. The thrust output indicated marginally lower values for BEM than for FVW. Looking at the root bending moment and tip deflection, the higher wind speed and wave elevation of the 18 m/s case However, the angle of attack saw significant discrepancies, with BEM showing greater variability, potentially leading to premature stall predictions. This highlights FVW's strength in tracking wake dynamics and capturing local feedback on blade aerodynamics.

The choice of turbulence model (NTM or ETM) was found to widen the range of differences between BEM and FVW in terms of power, torque, and thrust outputs, though it did not alter the overall trend. Regarding the root bending moment and tip deflection, the turbulence model used did not appear to influence the differences observed between the computational methods. Specifically, using ETM led to better alignment between BEM and FVW for the angle of attack compared to NTM. Increased turbulence intensity results in greater fluctuations in wind speed, which in turn amplifies differences in the angle of attack which was captured better by both methods than for the NTM.

What is the dependency on wind conditions?

A variety of wave conditions were simulated, differing in significant wave height, peak spectral period, and JONSWAP spectrum shape factor. It was challenging to pinpoint which parameter had the most influence on the differences between BEM and FVW.

Overall, the results indicated that waves have a minimal effect on the power, torque, and thrust outputs for both methods. This was confirmed by comparing DLC 1.1 and DLC 1.6 for the evaluated outputs. The same applied to root bending moment and tip deflection. Additionally, simulations of a bottom-fixed turbine at 18 m/s revealed similar differences between BEM and FVW as the floating case, suggesting that waves have little influence on the comparison between these models.

Hypothesis

The initial hypothesis was partially supported by the findings. Wind conditions had a greater impact on the differences between BEM and FVW than wave conditions. However, the best alignment between BEM and FVW was observed at the above-rated wind speed of 18 m/s for power, torque, and thrust. The angle of attack, however, showed the most significant differences at this high wind speed. This can be attributed to FVW's ability to model wake dynamics more precisely, which is especially important in capturing local aerodynamic conditions like angle of attack, where BEM's lack of wake structure falls short.

6

Recommendations

This chapter provides a retrospective analysis in Section 6.1, reflecting on the study's findings and methodologies. Finally, it offers recommendations for future research in Section 6.2.

6.1. Retrospection

In hindsight, several remarks can be made on the research which will be explained in this section.

Comparison with CFD or Experimental Results

In this study, the comparative assessment between a BEM and FVW model provided insights into their respective predictive capabilities for FOWTs. However, to ascertain the accuracy and fidelity of FVW relative to real-world conditions, it is of importance to include comparisons with CFD simulations. CFD simulations offer a high-fidelity approach by resolving the detailed flow physics around the turbine, thus serving as a benchmark. Another way to validate the BEM and FVW models is to compare it with experimental results.

Shear Exponent

In this study, a shear exponent α of 0.2 was used to represent the wind shear profile, which may not be fully representative of the actual offshore wind conditions. According to a DTU report on load cases [66], a shear exponent of 0.14 is typically applied for DLCs in offshore settings. The lower exponent of 0.14 is more realistic for offshore environments because it better reflects the more uniform wind profiles typically encountered over large bodies of water.

Influence of Parameters

Running fully coupled turbulent simulations of a FOWT presents a significant challenge when attempting to isolate and understand the effects of specific parameters. These simulations involve complex interactions among various physical phenomena, including aerodynamic forces, hydrodynamic influences, and control system responses. While this study provides a global overview of where the largest differences occur, a more detailed analysis is required to pinpoint which parameters are the root causes of these effects.

6.2. Future Work

A few recommendations can be done to extend this study and will be described in this section.

Number of Seeds & Simulations

To draw more robust and reliable conclusions, it is important to conduct multiple simulations per DLC using different random seeds. This methodology enhances the statistical significance of the results by ensuring that they are not influenced by a single set of initial conditions. It helps mitigate the impact of singular or rare events, which might otherwise skew the findings, providing a clearer picture of typical system behavior. Additionally, it captures the natural variability in wind and wave conditions, offering a comprehensive understanding of how the system performs under various realistic scenarios. This approach also improves the reliability of the conclusions through cross-validation and supports better design and optimization of FOWTs by ensuring that the designs are resilient across a range of conditions. Furthermore, it is critical for conducting thorough risk assessments, as a broader dataset allows for identifying potential failure modes and assessing the likelihood and impact of various risks, ultimately leading to safer and more efficient turbine designs.

Length of Simulations

To better assess the impact of waves and currents on FOWTs, running longer simulations could be beneficial. Longer simulation periods allow for a more comprehensive evaluation of the dynamic interactions between the wind turbine and the marine environment. This includes capturing the full range of wave and current conditions, such as long-period swells and tidal variations. This will provide insights into fatigue loading, which is critical for predicting the lifespan and maintenance needs of the turbine. Additionally, longer simulations enable the observation of slower-evolving phenomena, such as mooring line dynamics and long-term drift behavior, which are essential for ensuring the reliability and safety of FOWTs.

References

[1] F. Papi et al. “Quantifying the impact of modeling fidelity on different substructure concepts – Part 2: Code-to-code comparison in realistic environmental conditions”. In: *Wind Energy Science* 9.4 (2024), pp. 981–1004. DOI: `10.5194/wes-9-981-2024`.

[2] Jason M. Jonkman and Walter Musial. “Offshore Code Comparison Collaboration (OC3) for IEA Wind Task 23 Offshore Wind Technology and Deployment”. In: 2010. URL: `https://api.semanticscholar.org/CorpusID:108481126`.

[3] D. Micallef and A. Rezaeiha. “Floating offshore wind turbine aerodynamics: Trends and future challenges”. In: *Renewable and Sustainable Energy Reviews* 152 (2021). ISSN: 1364-0321. DOI: `https://doi.org/10.1016/j.rser.2021.111696`.

[4] T. Sebastian and M.A. Lackner. “Characterization of the unsteady aerodynamics of offshore floating wind turbines”. In: *Wind Energy* 16.3 (2013), pp. 339–352. DOI: `https://doi.org/10.1002/we.545`.

[5] J. Cruz and M. Atcheson. *Floating Offshore Wind Energy*. Springer Cham, 2016. DOI: `https://doi.org/10.1007/978-3-319-29398-1`.

[6] R. Farrugia, T. Sant, and D. Micallef. “A study on the aerodynamics of a floating wind turbine rotor”. In: *Renewable Energy* 86 (2016), pp. 770–784. ISSN: 0960-1481. DOI: `https://doi.org/10.1016/j.renene.2015.08.063`.

[7] J. Dong and A. Viré. “The aerodynamics of floating offshore wind turbines in different working states during surge motion”. In: *Renewable Energy* 195 (2022), pp. 1125–1136. ISSN: 0960-1481. DOI: `https://doi.org/10.1016/j.renene.2022.06.016`.

[8] J. Dong, A. Viré, and Z. Li. “Analysis the vortex ring state and propeller state of floating offshore wind turbines and verification of their prediction criteria by comparing with a CFD model”. In: *Renewable Energy* 184 (2022), pp. 15–25. ISSN: 0960-1481. DOI: `https://doi.org/10.1016/j.renene.2021.11.053`.

[9] R. Kyle, Y.C. Lee, and W.G. Früh. “Propeller and vortex ring state for floating offshore wind turbines during surge”. In: *Renewable Energy* 155 (2020), pp. 645–657. ISSN: 0960-1481. DOI: `https://doi.org/10.1016/j.renene.2020.03.105`.

[10] Y. Cai et al. “Aerodynamic analysis for different operating states of floating offshore wind turbine induced by pitching movement”. In: *Energy* 285 (2023). ISSN: 0360-5442. DOI: `https://doi.org/10.1016/j.energy.2023.129538`.

[11] J.B. de Vaal, M.O.L. Hansen, and T. Moan. “Effect of wind turbine surge motion on rotor thrust and induced velocity”. In: *Wind Energy* 17.1 (2014), pp. 105–121. DOI: `https://doi.org/10.1002/we.1562`.

[12] I. Bayati et al. “UNAFLOW project: UNsteady Aerodynamics of FLOating Wind turbines”. In: *Journal of Physics: Conference Series* 1037.7 (June 2018). DOI: `10.1088/1742-6596/1037/7/072037`. URL: `https://dx.doi.org/10.1088/1742-6596/1037/7/072037`.

[13] T. Sant et al. “Measurements and modelling of the power performance of a model floating wind turbine under controlled conditions”. In: *Wind Energy* 18.5 (2015), pp. 811–834. DOI: `https://doi.org/10.1002/we.1730`.

[14] X. Shen et al. “Study of the unsteady aerodynamics of floating wind turbines”. In: *Energy* 145 (2018), pp. 793–809. ISSN: 0360-5442. DOI: `https://doi.org/10.1016/j.energy.2017.12.100`.

[15] F. Taruffi, F. Novais, and A. Viré. “An experimental study on the aerodynamic loads of a floating offshore wind turbine under imposed motions”. In: *Wind Energy Science Discussions* (2023), pp. 1–24. DOI: `10.5194/wes-2023-86`.

[16] B. Stoevesandt et al. *Handbook of Wind Energy Aerodynamics*. Springer Nature, 2022. ISBN: 978-3-030-31306-7.

[17] J. G. Schepers. “Engineering models in wind energy aerodynamics: Development, implementation and analysis using dedicated aerodynamic measurements”. PhD thesis. TU Delft, 2012. DOI: `10.4233/uuid:92123c07-cc12-4945-973f-103bd744ec87`.

[18] D. Marten et al. *Qblade Documentation: Theory Guide*. URL: `https://docs.qblade.org/src/theory/index_th.html`.

[19] T. Sant. “Improving BEM-based Aerodynamic Models in Wind Turbine Design Codes”. PhD thesis. TU Delft, 2007.

[20] H. Glauert. “Airplane Propellers”. In: *Aerodynamic Theory*. Ed. by W. F. Durand. Vol. IV. Division L. New York: Springer, 1935, pp. 169–360. DOI: `10.1007/978-3-642-91487-4_3`.

[21] E. Branlard. *Wind Turbine Aeroydynamics and Voriticty-based Methods: Fundamentals and recent applications*. Springer, 2017. ISBN: 978-3-319-55163-0. DOI: `https://doi.org/10.1007/978-3-319-5516407`.

[22] J. N. Sørensen. *General Momentum Theory for Horizontal Axis Wind Turbines*. Springer Cham, 2015. DOI: `https://doi.org/10.1007/978-3-319-22114-4`.

[23] G.A.M. van Kuik. *The Fluid Dynamic Basis for Actuator Disc and Rotor Theories*. IOS Press BV, 2022. ISBN: 978-1-64368-279-2. DOI: `10.3233/STAL9781643682792`.

[24] J. Ledoux, S. Riffo, and J. Salomon. “Analysis of the Blade Element Momentum Theory”. In: *SIAM Journal on Applied Mathematics* 81.6 (2021), pp. 2596–2621. DOI: `10.1137/20M133542X`. eprint: `hal-02550763v2`.

[25] J.N. Sørensen. “4 - Wind turbine wakes and wind farm aerodynamics”. In: *Wind Energy Systems*. Woodhead Publishing Series in Energy. Woodhead Publishing, 2011, 112–e131. ISBN: 978-1-84569-580-4. DOI: `https://doi.org/10.1533/9780857090638.1.112`.

[26] F. Papi et al. “Going Beyond BEM with BEM: an Insight into Dynamic Inflow Effects on Floating Wind Turbines”. In: *Wind Energy Science Discussions* (2023). DOI: `10.5194/wes-2023-109`.

[27] S. Perez-Becker et al. “Is the Blade Element Momentum theory overestimating wind turbine loads? - An aeroelastic comparison between OpenFAST’s AeroDyn and QBlade’s Lifting-Line Free Vortex Wake method”. In: *Wind Energy Science* 5.2 (2020), pp. 721–743. DOI: `10.5194/wes-5-721-2020`.

[28] W.Z. Shen, R. Mikkelsen, and J.N. Sørensen. “Tip Loss Corrections for Wind Turbine Computations”. In: *Wind Energy* 8.4 (2005), pp. 457–475. DOI: `10.1002/we.153`.

[29] S. Hauptmann et al. “Comparison of the lifting-line free vortex wake method and the blade-element-momentum theory regarding the simulated loads of multi-MW wind turbines”. In: *Journal of Physics: Conference Series* 555.1 (Dec. 2014). DOI: `10.1088/1742-6596/555/1/012050`. URL: `https://dx.doi.org/10.1088/1742-6596/555/1/012050`.

[30] Herman Snel and J Schepers. “Investigation and modelling of dynamic inflow effects”. In: (Jan. 1993).

[31] R. Bergua et al. “OC6 project Phase III: validation of the aerodynamic loading on a wind turbine rotor undergoing large motion caused by a floating support structure”. In: *Wind Energy Science* 8.4 (2023), pp. 465–485. DOI: `10.5194/wes-8-465-2023`.

[32] H. Glauert. *The Analysis of Experimental Results in the Windmill Brake and Vortex Ring States of an Airscrew*. Tech. rep. R & M No. 1026. British ARC, 1926.

[33] H. Himmelskamp. “Profile Investigations on a Rotating Aircrew”. Reports and Translations No. 832, Sept. 1947. PhD thesis. University of Gottingen, 1945.

[34] H. Snel, R. Houwink, and W. J. Piers. “Sectional Prediction of 3D Effects for Separated Flow on Rotating Blades”. In: (1993).

[35] J. G. Leishman and T. S. Beddoes. “A semi-empirical model for dynamic stall”. In: *Journal of the American Helicopter Society* 34 (1989), pp. 3–17. DOI: `10.4050/JAHS.34.3.3`.

[36] S. Øye. “Dynamic stall simulated as time lag of separation”. In: (1991).

[37] D. Marten et al. “Implementation, Optimization, and Validation of a Nonlinear Lifting Line-Free Vortex Wake Module Within the Wind Turbine Simulation Code qblade”. In: *Journal of Engineering for Gas Turbines and Power* 138.7 (Dec. 2015), p. 072601. ISSN: 0742-4795. DOI: `10.1115/1.4031872`.

[38] J. Dong et al. “A Modified Free Wake Vortex Ring Method for Horizontal-Axis Wind Turbines”. In: *Energies* 12.20 (2019). DOI: `10.3390/en12203900`.

[39] J.G. Schepers et al. “Final results from the EU project AVATAR: Aerodynamic modelling of 10 MW wind turbines”. In: *Journal of Physics: Conference Series* 1037.2 (June 2018), p. 022013. DOI: `10.1088/1742-6596/1037/2/022013`.

[40] N. Ramos García et al. “Investigation of the floating IEA Wind 15 MW RWT using vortex methods Part I: Flow regimes and wake recovery”. In: *Wind Energy* 25.3 (2021), pp. 468–504. ISSN: 10991824, 10954244. DOI: `10.1002/we.2682`.

[41] K. Boorsma et al. “Progress in validation of rotor aerodynamic codes using field data”. In: *Wind Energy Science Discussions* (2022), pp. 1–31.

[42] S. Becker et al. *FLOATECH D2.2. Validation Report of QBlade-Ocean*. Tech. rep. 2022.

[43] R. Behrens de Luna et al. “Comparison of different fidelity aerodynamic solvers on the IEA 10 MW turbine including novel tip extension geometries”. In: *Journal of Physics: Conference Series* 2265.3 (May 2022), p. 032002. DOI: `10.1088/1742-6596/2265/3/032002`.

[44] F. Papi et al. “A Code-to-Code Comparison for Floating Offshore Wind Turbine Simulation in Realistic Environmental Conditions: Quantifying the Impact of Modeling Fidelity on Different Substructure Concepts”. In: *Wind Energy Science Discussions* (2023). DOI: `10.5194/wes-2023-107`.

[45] R. Behrens de Luna et al. “Quantifying the impact of modeling fidelity on different substructure concepts for floating offshore wind turbines – Part 1: Validation of the hydrodynamic module QBlade-Ocean”. In: *Wind Energy Science* 9.3 (2024), pp. 623–649. DOI: `10.5194/wes-9-623-2024`.

[46] T. Leu et al. “ASSESSMENT OF IEC 61400-1 NORMAL TURBULENCE MODEL FOR WIND CONDITIONS IN TAIWAN WEST COAST AREAS”. In: *International Journal of Modern Physics: Conference Series* 34 (2014), p. 1460382. DOI: `10.1142/S2010194514603822`.

[47] T. Ishihara, A. Yamaguchi, and M. Sarwar. “A Study of the Normal Turbulence Model in IEC 61400-1”. In: *Wind Engineering* 36 (Dec. 2012), pp. 759–766. DOI: `10.1260/0309-524X.36.6.759`.

[48] J. S. Moon et al. “On the Use of Site Data to Define Extreme Turbulence Conditions for Wind Turbine Design [39]”. In: *Journal of Solar Energy Engineering* 136 (Nov. 2014). DOI: `10.1115/1.4028721`.

[49] Á. Hannesdóttir, M. Kelly, and N. Dimitrov. “Extreme wind fluctuations: joint statistics, extreme turbulence, and impact on wind turbine loads”. In: *Wind Energy Science* 4.2 (2019), pp. 325–342. DOI: `10.5194/wes-4-325-2019`.

[50] P. Webb. *Introduction to Oceanography*. Cengage Learning, 2004. URL: `https://rwu.pressbooks.pub/webboceanography/`.

[51] L. Holthuijsen. “Waves in Oceanic and Coastal Waters”. In: *Cambridge University Press* (Jan. 2007), p. 404. DOI: `10.2277/0521860288`.

[52] K. Hasselmann et al. “Measurements of wind-wave growth and swell decay during the Joint North Sea Wave Project (JONSWAP)”. In: *Ergänzungsheft zur Deutschen Hydrographischen Zeitschrift Reihe, A* 8.12 (1973), p. 95.

[53] Subrata K. Chakrabarti. “Chapter 3 - Ocean Environment”. In: *Handbook of Offshore Engineering*. Ed. by SUBRATA K. CHAKRABARTI. London: Elsevier, 2005, pp. 79–131. ISBN: 978-0-08-044381-2. DOI: `https://doi.org/10.1016/B978-008044381-2.50006-0`.

[54] C. Allen, A. Viselli, et al. *Definition of the UMaine VolturnUS-S Reference Platform Developed for the IEA Wind 15-Megawatt Offshore Reference Wind Turbine*. Tech. rep. NREL, 2020.

[55] E. Gaertner et al. *IEA Wind TCP Task 37: Definition of the IEA 15-Megawatt Offshore Reference Wind Turbine*. Tech. rep. IEA, Mar. 2020. DOI: `10.2172/1603478`.

[56] D. Marten. “QBlade: A Modern Tool for the Aeroelastic Simulation of Wind Turbines”. PhD Thesis. TU Berlin, 2020.

[57] A. van Garrel. *Development of a Wind Turbine Aerodynamics Simulation Module*. Tech. rep. ECN, 2003.

[58] Claudio Tavares da Silva and Mauricio Donadon. "Unsteady Blade Element-Momentum Method Including Returning Wake Effects". In: *Journal of Aerospace Technology and Management* 5 (Mar. 2013). DOI: `10.5028/jatm.v5i1.163`.

[59] L. C. Henriksen, M. H. Hansen, and N. K. Poulsen. "A simplified dynamic inflow model and its effect on the performance of free mean wind speed estimation". In: *Wind Energy* 16.8 (2013), pp. 1213–1224. DOI: `https://doi.org/10.1002/we.1548`.

[60] H. A. Madsen et al. "Implementation of the blade element momentum model on a polar grid and its aeroelastic load impact". In: *Wind Energy Science* 5.1 (2020), pp. 1–27. DOI: `10.5194/wes-5-1-2020`.

[61] D. van den Berg, D. de Tavernier, and J.-W. van Wingerden. "The dynamic coupling between the pulse wake mixing strategy and floating wind turbines". In: *Wind Energy Science* 8.5 (2023), pp. 849–864. DOI: `10.5194/wes-8-849-2023`.

[62] C. Bak et al. *Description of the DTU 10 MW Reference Wind Turbine*. Tech. rep. Wind Energy. Technical University of Denmark, 2013. URL: `http://orbit.dtu.dk/files/55645274/The_DTU_10MW_Reference_Turbine_Christian_Bak.pdf`.

[63] Abdolrahim Rezaeiha, Ricardo Pereira, and Marios Kotsonis. "Fluctuations of angle of attack and lift coefficient and the resultant fatigue loads for a large Horizontal Axis Wind turbine". In: *Renewable Energy* 114 (Aug. 2017), pp. 904–916. DOI: `10.1016/j.renene.2017.07.101`.

[64] J. D. Ahrens et al. "Predicting the Onset of Dynamic Stall on Large Wind Turbines". In: *Wind Energy Science Discussions* 2023 (2023), pp. 1–17. DOI: `10.5194/wes-2023-159`.

[65] Peter Fuglsang, Ioannis Antoniou, and Kristian Dahl. "Wind tunnel tests of the FFA-W3-241, FFA-W3-301 and NACA 63-430 airfoils". In: (Jan. 1998).

[66] A. Natarajan, M. H. Hansen, and S. Wang. *Design Load Basis for Offshore Wind Turbines*. Tech. rep. E-0133. DTU Wind Energy, 2016.

A

Hub Height Wind Speed

This appendix includes plots of the wind speed at hub height for each simulation, organized by design load case. The wind speed is averaged over 5-second intervals to produce smoother plots. The results demonstrate that there is virtually no difference between BEM and FVW in terms of hub height wind speed.

A.1. DLC 1.1

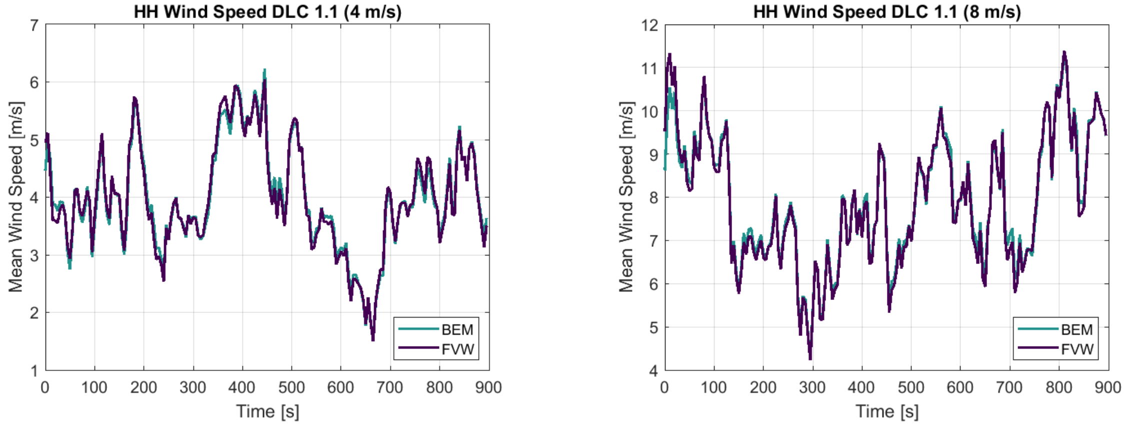

(a) Mean HH wind speed 4 m/s.

(b) Mean HH wind speed 8 m/s.

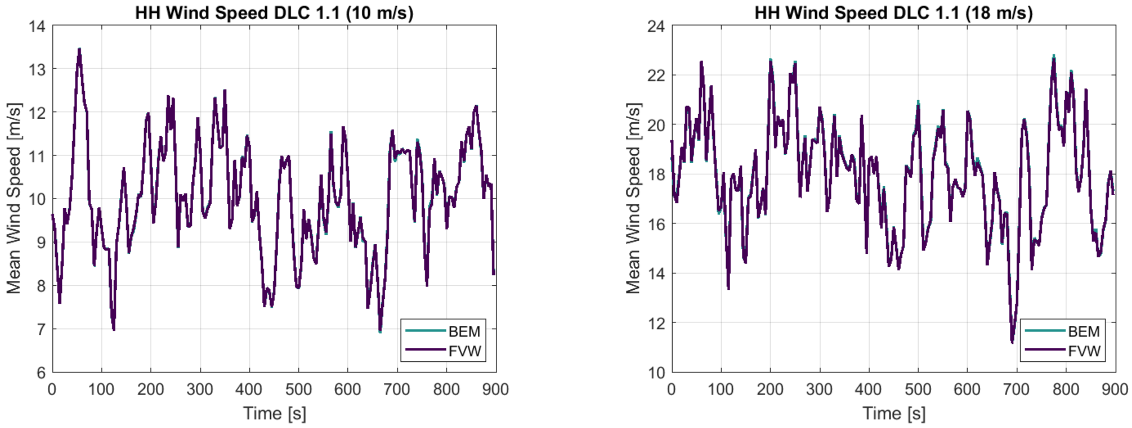

(c) Mean HH wind speed 10 m/s.

(d) Mean HH wind speed 18 m/s.

Figure A.1: HH wind speed for different simulations of DLC 1.1.

A.2. DLC 1.3

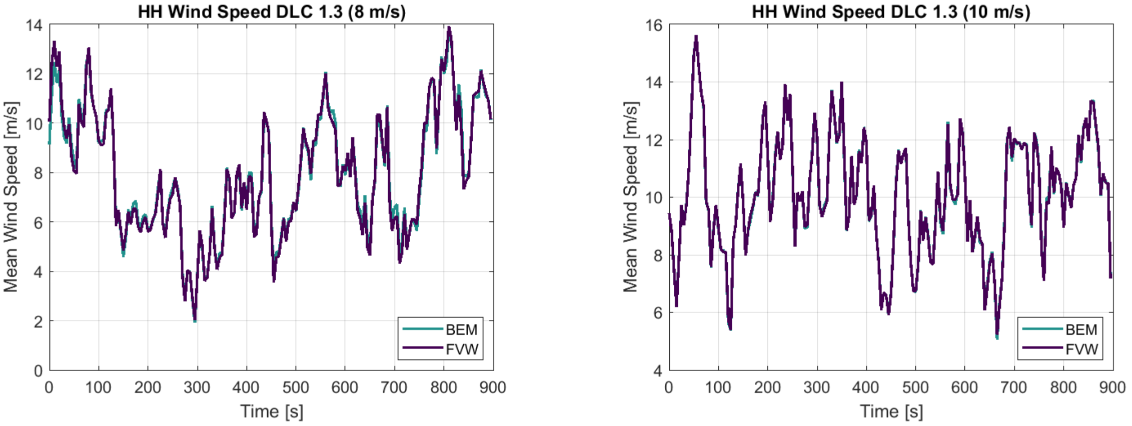

(a) Mean HH wind speed 8 m/s.

(b) Mean HH wind speed 10 m/s.

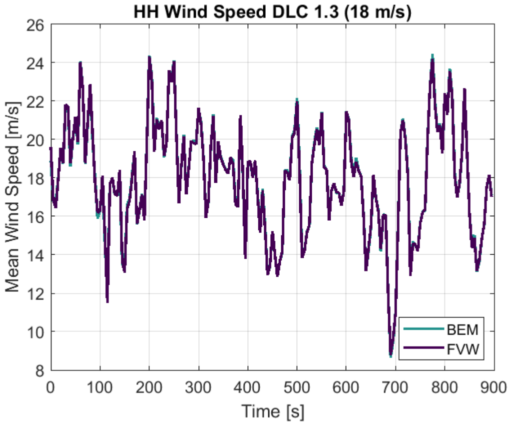

(c) Mean HH wind speed 18 m/s.

Figure A.2: HH wind speed for different simulations of DLC 1.3.

A.3. DLC 1.6

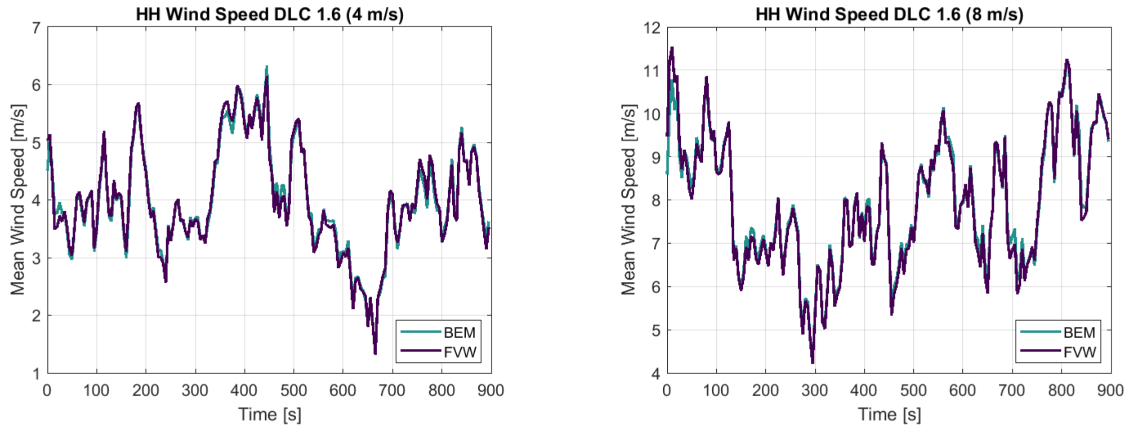

(a) Mean HH wind speed 4 m/s.

(b) Mean HH wind speed 8 m/s.

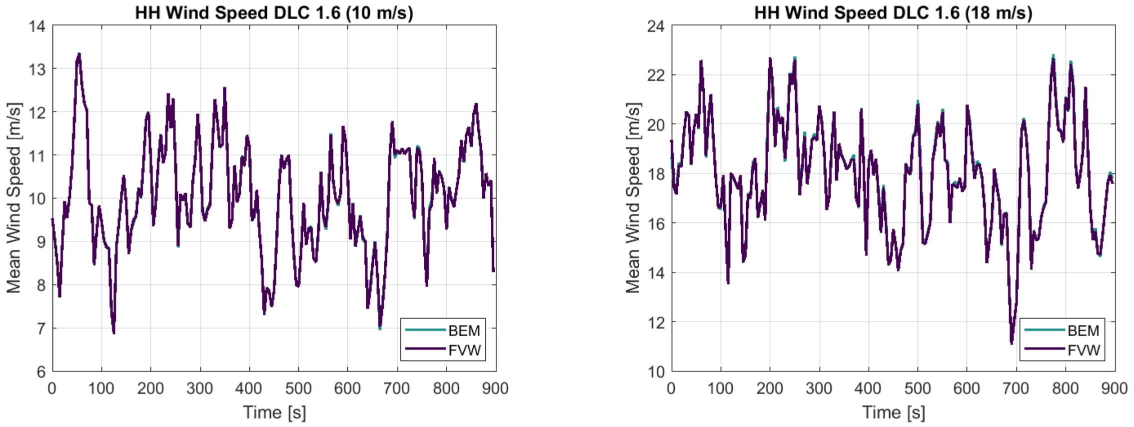

(c) Mean HH wind speed 10 m/s.

(d) Mean HH wind speed 18 m/s.

Figure A.3: HH wind speed for different simulations of DLC 1.6.

A.4. DLC 6.3

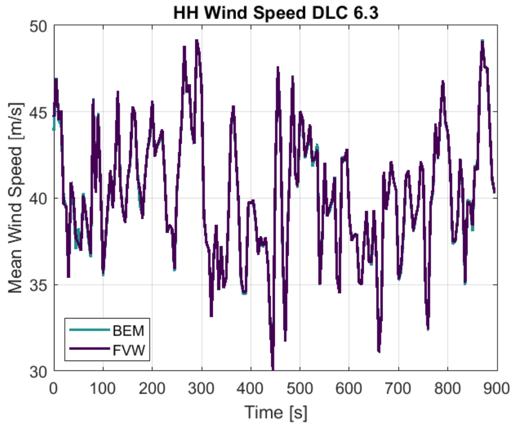

Figure A.4: HH wind speed DLC 6.3.

B

Pitch Angle

This appendix includes plots of pitch angle for each simulation, organized by design load case. The wind speed is averaged over 5-second intervals to produce smoother plots. The result show how each computational method could have different reactions in controller behaviour.

B.1. DLC 1.1

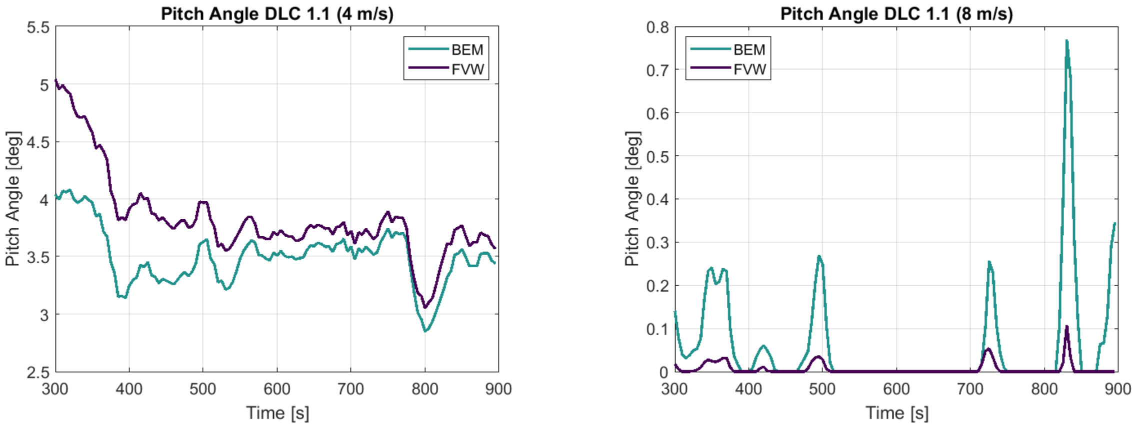

(a) Pitch angle 4 m/s.

(b) Pitch angle 8 m/s.

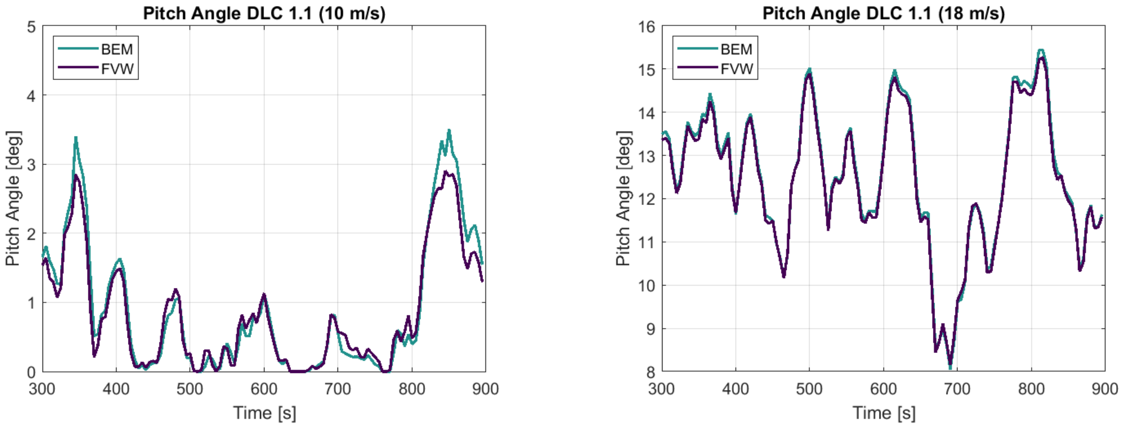

(c) Pitch angle 10 m/s.

(d) Pitch angle 18 m/s.

Figure B.1: Pitch angles for different simulations of DLC 1.1.

B.2. DLC 1.3

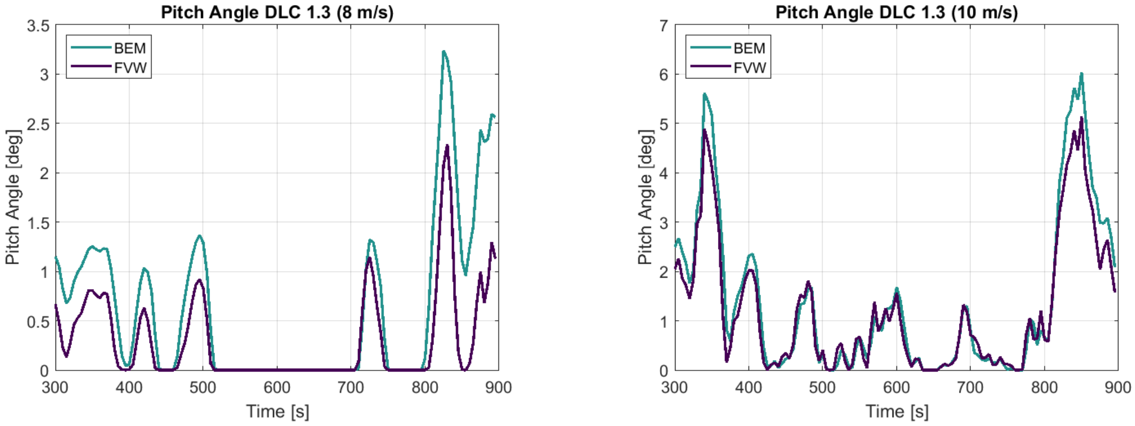

(a) Pitch angle 8 m/s.

(b) Pitch angle 10 m/s.

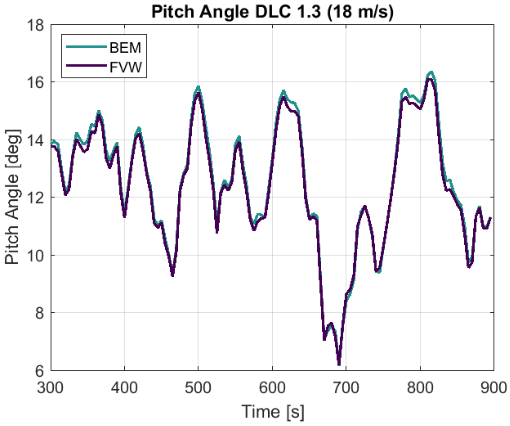

(c) Pitch angle 18 m/s.

Figure B.2: Pitch angles for different simulations of DLC 1.3.

B.3. DLC 1.6

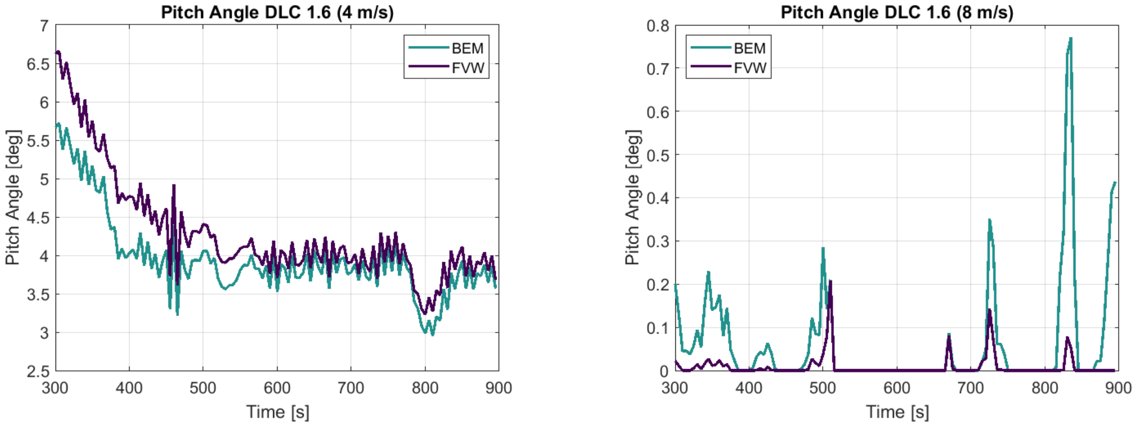

(a) Pitch angle 4 m/s.

(b) Pitch angle 8 m/s.

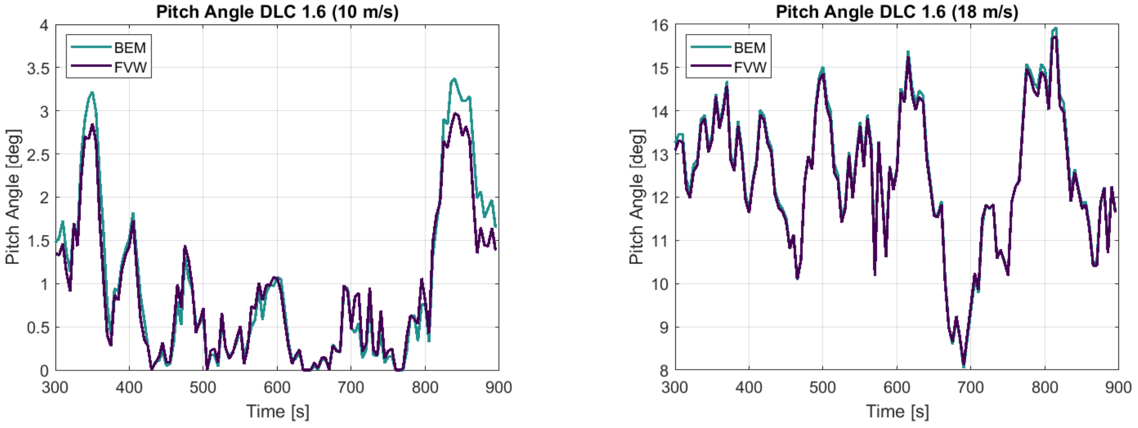

(c) Pitch angle 10 m/s.

(d) Pitch angle 18 m/s.

Figure B.3: Pitch angles for different simulations of DLC 1.6.

B.4. DLC 6.3

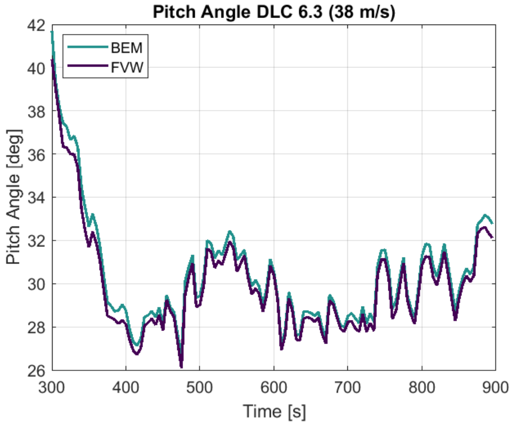

Figure B.4: Pitch angle DLC 6.3.

C

Torque

This appendix includes plots of the torque for each simulation, organized by design load case. The wind speed is averaged over 5-second intervals to produce smoother plots. The result show how each computational method could have different reactions in controller behaviour.

C.1. DLC 1.1

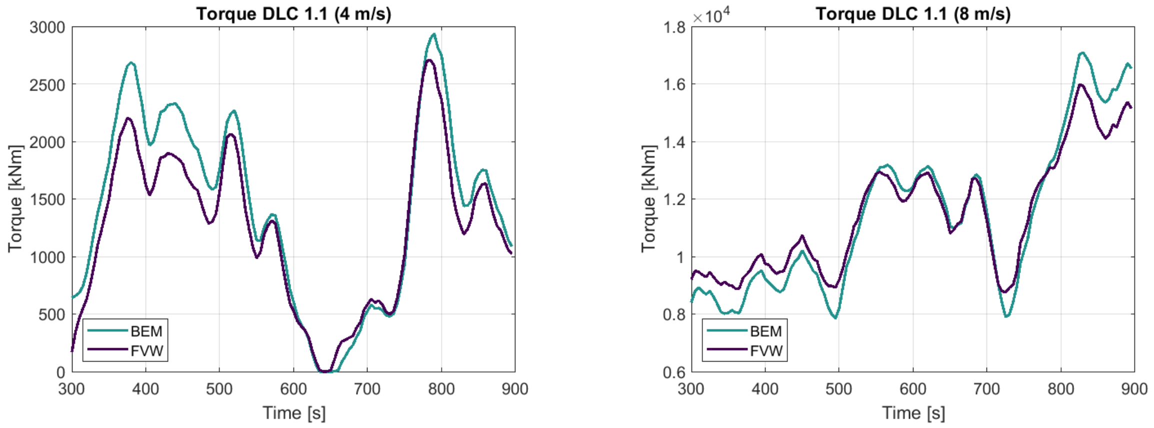

(a) Torque 4 m/s.

(b) Torque 8 m/s.

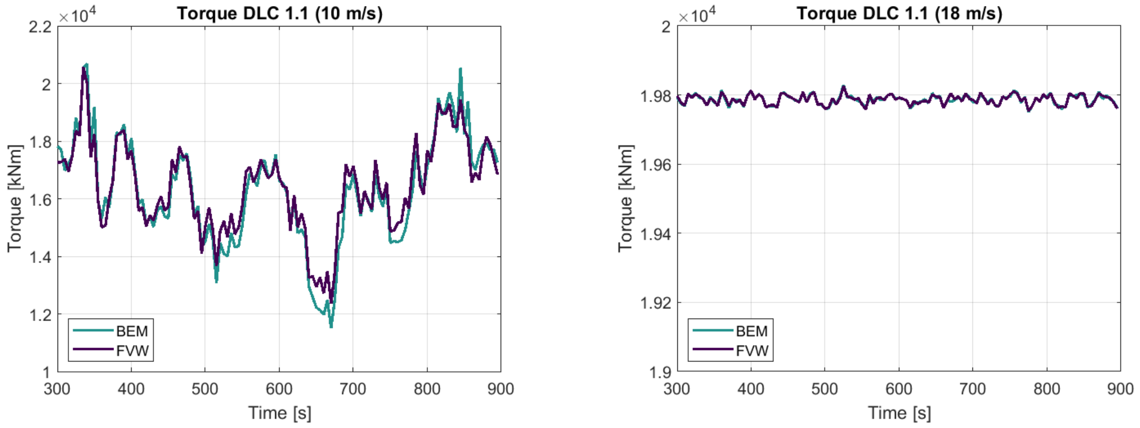

(c) Torque 10 m/s.

(d) Torque 18 m/s.

Figure C.1: Torque for different simulations of DLC 1.1.

C.2. DLC 1.3

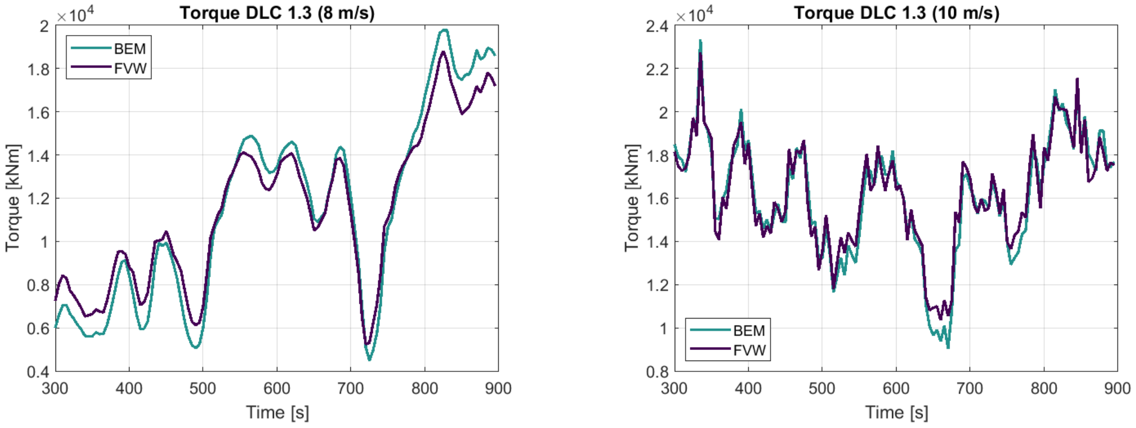

(a) Torque 8 m/s.

(b) Torque 10 m/s.

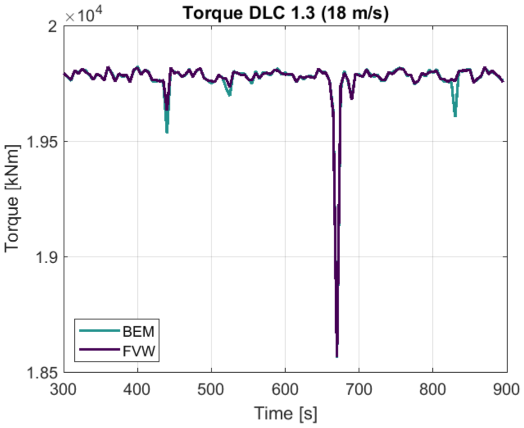

(c) Torque 18 m/s.

Figure C.2: Torque for different simulations of DLC 1.3.

C.3. DLC 1.6

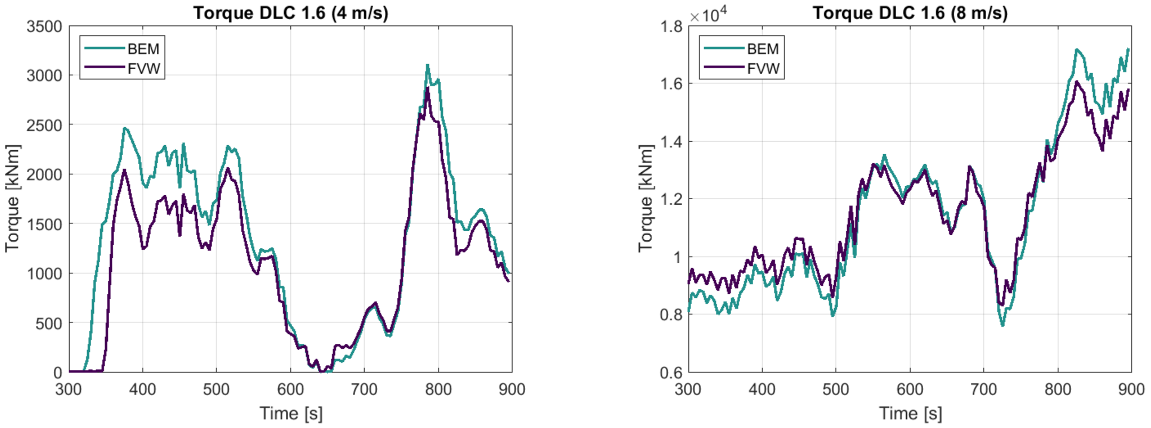

(a) Torque 4 m/s. **(b)** Torque 8 m/s.

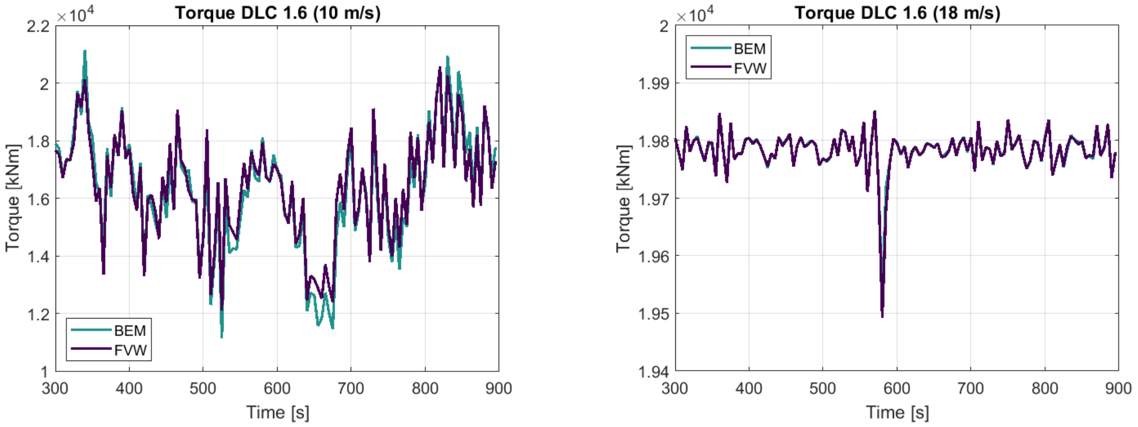

(c) Torque 10 m/s. **(d)** Torque 18 m/s.

Figure C.3: Torque for different simulations of DLC 1.6.

C.4. DLC 6.3

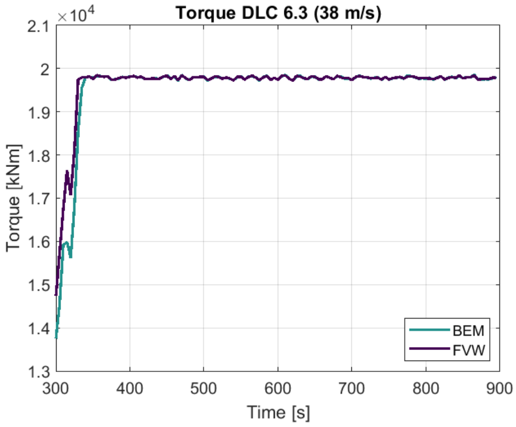

Figure C.4: Torque DLC 6.3.